REPORT DOCUMENTATION PAGE

The public reporting burden for this collection of information is estimated to average 1 hour per response, including the time for reviewing instructions, searching existing data sources, gathering and maintaining the data needed, and completing and reviewing the collection of information. Send comments regarding this burden estimate or any other aspect of this collection of information, including suggestions for reducing the burden, to the Department of Defense, Executive Service Directorate (0704-0188). Respondents should be aware that notwithstanding any other provision of law, no person shall be subject to any penalty for failing to comply with a collection of information if it does not display a currently valid OMB control number.

PLEASE DO NOT RETURN YOUR FORM TO THE ABOVE ORGANIZATION.

1. REPORT DATE (DD-MM-YYYY)	2. REPORT TYPE	3. DATES COVERED (From - To)
24-03-2009	Final Report	December 2005 - November 2008

4. TITLE AND SUBTITLE
Evaluation of Acoustic Propagation Paths into the Human Head

5a. CONTRACT NUMBER

5b. GRANT NUMBER
FA9550-06-1-0128

5c. PROGRAM ELEMENT NUMBER

6. AUTHOR(S)
O'Brien, William D., Jr.

5d. PROJECT NUMBER

5e. TASK NUMBER

5f. WORK UNIT NUMBER

7. PERFORMING ORGANIZATION NAME(S) AND ADDRESS(ES)
The Board of Trustees of the University of Illinois
506 S. Wright Street
Urbana, IL 61801

8. PERFORMING ORGANIZATION REPORT NUMBER

9. SPONSORING/MONITORING AGENCY NAME(S) AND ADDRESS(ES)
USAF, AFRL
AF Office of Scientific Research
875 N. Randolph Street, Room 3112
Arlington, VA 22203
Dr. Willard Larkin/NL

10. SPONSOR/MONITOR'S ACRONYM(S)
AFOSR

11. SPONSOR/MONITOR'S REPORT NUMBER(S)

12. DISTRIBUTION/AVAILABILITY STATEMENT
Approved for public release

AFRL-OSR-VA-TR-2012- 0024

13. SUPPLEMENTARY NOTES

14. ABSTRACT
In summary, the highly interdisciplinary program has addressed successfully the challenging technical goals set forth to develop and validate an acoustic wave propagation model using well understood and documented computational techniques that track an air-borne incident acoustic wave propagated around, into and in the human head. A finite element model was formulated for simulating the acoustic wave propagation into concentric spheres. This model was verified against the closed form solution of the plane wave propagation into concentric fluid spheres. A ray tracing method was developed and verified to visualize the acoustic wave propagation pathways from a scalar pressure field. Finally, the occlusion effect provides a relatively robust phenomenon to compare the computational findings with the behavioral and functional findings; the occlusion effect contour (or difference score) between the open and occluded ear show a similar trend between the computational findings and the behavioral and functional findings. In conclusion, the computational approach, utilizing fluid elements, provides very good agreement with human subject findings.

15. SUBJECT TERMS
acoustic propagation paths; human head; computational techniques; ray tracing methods; human subjects

16. SECURITY CLASSIFICATION OF:			17. LIMITATION OF ABSTRACT	18. NUMBER OF PAGES	19a. NAME OF RESPONSIBLE PERSON
a. REPORT	b. ABSTRACT	c. THIS PAGE	UU		William D. O'Brien, Jr.
					19b. TELEPHONE NUMBER (Include area code) 217-333-2407

University of Illinois
at Urbana-Champaign

Bioacoustics Research Laboratory

Department of Electrical and Computer Engineering
The Beckman Institute for Advanced Science and Technology
405 North Mathews Avenue
Urbana, Illinois 61801

Office: (217) 333-1640
FAX: (217) 244-0105
Email: sjc@uiuc.edu

March 31, 2009

Willard Larkin
AFOSR/NL
875 North Randolph Street
Arlington, VA 22203

Dear Willard,

Please find enclosed a DVD and a paper copy of Bill O'Brien's final report on his grant
AFOSR FA9550-06-1-0128.

Bill uploaded the report to the AFOSR website, but also wanted you to have a copy.

Best regards,

Sue Clay
Administrative Assistant

FINAL REPORT

"Evaluation of Acoustic Propagation Paths into the Human Head"
Grant Number: FA9550-06-1-0128
Program Manager: Dr. Willard Larkin, AFOSR/NL
Reporting Period: December 1, 2005 – November 30, 2008
Report Date: February 24, 2009

Prepared by:
William D. O'Brien, Jr.
Department of Electrical and Computer Engineering
University of Illinois at Urbana-Champaign
405 N. Mathews
Urbana, IL 61801
Phone: 217/333-2407
FAX: 217/244-0105
email: wdo@uiuc.edu

1. INTRODUCTION

This is the Final Report for the grant "Evaluation of Acoustic Propagation Paths into the Human Head," Grant Number: FA9550-06-1-0128, for the period between December 1, 2005 and November 30, 2008. The Air Force Program Manager is Dr. Willard Larkin, and the Principal Investigator at University of Illinois at Urbana–Champaign is Professor William D. O'Brien, Jr.

The overall objective of the program was the further development and validation of an acoustic wave propagation model using well understood and documented computational techniques that track an air-borne incident acoustic wave propagated around, into and in the human head. The validation testing of the computational model involved human subject testing. The theoretical model provided a known fundamental basis, and the experiment provided the evidence to evaluate the model. The goal to further development and validation of an acoustic wave propagation model has been achieved.

In summary, the highly interdisciplinary program has addressed successfully the challenging technical goals set forth to develop and validate an acoustic wave propagation model using well understood and documented computational techniques that track an air-borne incident acoustic wave propagated around, into and in the human head. A finite element model was formulated for simulating the acoustic wave propagation into concentric spheres. This model was verified against the closed form solution of the plane wave propagation into concentric fluid spheres. A ray tracing method was developed and verified to visualize the acoustic wave propagation pathways from a scalar pressure field. Finally, the occlusion effect provides a relatively robust phenomenon to compare the computational findings with the behavioral and functional findings; the occlusion effect

- 1 -

contour (or difference score) between the open and occluded ear show a similar trend between the computational findings and the behavioral and functional findings. In conclusion, the computational approach, utilizing fluid elements, provides very good agreement with human subject findings.

2. ACOUSTIC WAVE PROPAGATION MODEL

This section presents the numerical simulation of evaluating pathways of bone conducted sound. Two separate algorithms have been developed in order to model the physical effects of acoustic energy interacting with bone, soft tissue and hearing protection devices. The original method is a pressure-based formulation of the acoustic wave equation. The pressure-based method simulates only sound wave propagation through inhomogeneous fluid media. The second method is a displacement-based approach that simulates elastodynamic wave propagation through a solid medium and/or a fluid-solid interface. Both algorithms are based on a 3D finite element (FE) matrix formulation of the acoustic wave equation. Novel aspects of the implementation include the fact that the program accepts stacks of digital images to form the 3D input volume, the program uses Message Passing Interface (MPI) directives in order to run on an intensively parallel cluster, the program uses a uniform grid and has special memory saving techniques making it possible to simulate relatively large areas. The program also uses an explicit time-domain algorithm, such that no matrix inversion is required, and multiple frequencies can be evaluated. Also a Mur-Engquidst absorbing boundary condition is imposed on the outer boundaries of the simulation area so that the modeling of radiation and scattering effects from the skull are more accurate. The pressure-based algorithm is used to simulate the corresponding experiments on live human subjects whereby sound is transmitted though the skull via head mounted vibrators.

2.1. Theoretical aspects (Pressure-based method)

The acoustic wave equation is given as

$$\nabla \cdot \frac{1}{\rho(r)} \nabla p - \frac{1}{\rho(r)c^2(r)} \frac{\partial^2 p}{\partial t^2} + \frac{\partial}{\partial t} \nabla \cdot \frac{2c(r)\alpha(r)}{\rho(r)} \nabla p = 0, \tag{1}$$

and mathematically characterizes the pressure, p, as it evolves in both space, r, and time,

t, due to input pressures on boundaries and interfaces. In this equation $\rho(r)$ is a spatially dependent density, $c(r)$ is the sound speed and $\square(r)$ is an attenuation coefficient. This is an inhomogeneous wave equation with no input driving force on the right hand side. All inputs are represented by pressures on the surface of one of the modeled structures. The finite element discretization converts this spatially continuous wave equation into one in which the pressure is described at discrete points in space indicated by p_i in the following relation

$\alpha(r)$

$$\left[K_{FS}\right]\{p_i\} - \left[M\right]\left\{\frac{\partial^2 p_i}{\partial t^2}\right\} + \tau_i\left[K_{FS}\right]\left\{\frac{\partial p_i}{\partial t}\right\} = \left[Q_F\right]. \tag{2}$$

The simulated area is sliced into smaller individual elements. For the 3D model these elements are cubes with 8 nodes, one at each corner. The nodes are numbered 0 through N-1 and $\{p_i\}$ is a vector of length N representing the pressure at all the nodes in the mesh. For the initial program attenuation is not included and the inertial term time derivative is approximated with a centered difference equation such that

$$\frac{\partial^2 p_i}{\partial t^2} \approx \frac{p_i^{t+\Delta t} - 2p_i^t + p_i^{t-\Delta t}}{\Delta t^2}. \tag{3}$$

Insertion of this formula into equation 2 and solving for $\{p_i\}^{t+\square}$ yields

$$\left\{p_i\right\}^{t+\Delta t} = \left[M\right]^{-1}\left[K_{FS}\right]\{p_i\}^t + 2\left\{p_i\right\}^t - \left\{p_i\right\}^{t-\Delta t} - \left[Q_F\right]. \tag{4}$$

In this formula both the stiffness matrix $[K_{stiff}]$ and the mass matrix $[M]$ are N x N matrices which relate the node i to every other node in the mesh while $[Q]$ is a row vector. These matrices are defined by

$$K_{FS} = -\frac{1}{\rho_j}\int \nabla N_j \nabla N_i \, dV \qquad M = \frac{1}{\rho_j c_j}\int N_j N_i \, dV \qquad Q_F = \frac{1}{\rho_j}\int N_j \frac{\partial p_i}{\partial n} \, dS \tag{5}$$

in which N_j and N_i are linear interpolation functions defined at the nodes. The numerical algorithm implements this equation. Because first order brick elements in the FE mesh are used each row has a non-zero value for only the ij entry for which j is one of the 26 nodes surrounding i resulting in sparse matrices for stiffness and mass. Through diagonalization of the mass matrix, $[M]$, matrix inversion is avoided and a purely explicit time-stepping scheme is achieved.

Through the use of benchmarking techniques, it has been determined that at least 40 nodes per wavelength are required to accurately model a pressure wave. This means for an input pressure signal centered around 4 kHz propagating through air with a sound speed 333 m/s the minimum wavelength, assuming a bandwidth of 2 kHz, is 333/5000 = 6.6 cm. Therefore approximately $400^3 = 64$ million nodes would be required in order to simulate an area 60 x 60 x 60 cm [0.60/(0.066/40)=400]. In order to not store a matrix of

27 x 64 million only unique rows of the stiffness matrix are formed and stored. The process is described in more detail in Section 2.4.

2.2. Theoretical aspects (Displacement-based approach)

The pressure-based formulation does not account for shear phenomena found in solids such as bone, helmets or other protective gear. In order to account for the solid shear effects the elastic pressure wave within solids must be modeled along with the fluid/structure interface. The two main methods for extending the finite-element code to include solid shear effects is to used a pressure-based equation in the fluid and a displacement-based method in the solid or to use a pure displacement-based method throughout the both fluid and solid. In the mixed pressure/displacement formulation the loading between the fluid and solid must be satisfied by enforcing continuity of pressure and displacement along all interfaces between the two types of media. The disadvantage of this method is that the all nodes along fluid-solid interfaces must be identified and stored and a separate interface matrix must be assembled and solved. In pure displacement-based equations, particle displacement is solved for both the fluid and solid media and therefore continuity conditions at fluid-solid interfaces are automatically satisfied. The disadvantages of this method are that 1) because displacement is a vector quantity 3 degrees of freedom must be stored for both the fluid and solid and 2) the irrotation of displacement in the fluid $\nabla \times \vec{u} = 0$, is not automatically ensured. For this project the displacement-based method is adopted as it is much easier to code, the additional memory requirements are incremental for the high performance computers and there are documented methods for controlling the rotation problem.

Displacement wave propagation through solids is modeled via the elastic wave equation written succinctly as (Auld, 1990; Eq. 6.5)

$$\nabla_s \bullet \left(C : \nabla_s \vec{u} \right) = \rho \frac{\partial^2 \vec{u}}{\partial t^2} \tag{6}$$

in which $\vec{u}$ is a vector of the displacements in the x, y and z directions, C is a 6 x 6 matrix of the elastic coefficients and ∇_s is a strain operator written out as

$$\nabla_s = \begin{bmatrix} \frac{\partial}{\partial x} & 0 & 0 & 0 & \frac{\partial}{\partial z} & \frac{\partial}{\partial y} \\ 0 & \frac{\partial}{\partial y} & 0 & \frac{\partial}{\partial z} & 0 & \frac{\partial}{\partial x} \\ 0 & 0 & \frac{\partial}{\partial z} & \frac{\partial}{\partial y} & \frac{\partial}{\partial x} & 0 \end{bmatrix}. \tag{7}$$

If one were to expand the elastic wave equation to show individual terms the result would be three equations with multiple stiffness terms. For instance the simplest

solid is the cubic type for which there are only three independent values for the elastic stiffness constants namely c_{11}, c_{12} and c_{44}. Expanded the wave equation appears as

$$\left(c_{11}\frac{\partial^2}{\partial x^2} + c_{44}\left[\frac{\partial^2}{\partial y^2} + \frac{\partial^2}{\partial z^2} \right] \right) u_x + \left(c_{12} + c_{44} \right)\frac{\partial^2 u_y}{\partial x \partial y} + \left(c_{12} + c_{44} \right)\frac{\partial^2 u_z}{\partial x \partial z} - \rho\frac{\partial^2 u_x}{\partial t^2} = 0 \qquad (8a)$$

$$\left(c_{12} + c_{44} \right)\frac{\partial^2 u_x}{\partial x \partial y} + \left(c_{11}\frac{\partial^2}{\partial y^2} + c_{44}\left[\frac{\partial^2}{\partial x^2} + \frac{\partial^2}{\partial z^2} \right] \right) u_y + \left(c_{12} + c_{44} \right)\frac{\partial^2 u_z}{\partial y \partial z} - \rho\frac{\partial^2 u_y}{\partial t^2} = 0 \qquad (8b)$$

$$\left(c_{12} + c_{44} \right)\frac{\partial^2 u_x}{\partial x \partial z} + \left(c_{12} + c_{44} \right)\frac{\partial^2 u_y}{\partial y \partial z} + \left(c_{11}\frac{\partial^2}{\partial z^2} + c_{44}\left[\frac{\partial^2}{\partial y^2} + \frac{\partial^2}{\partial x^2} \right] \right) u_z + -\rho\frac{\partial^2 u_z}{\partial t^2} = 0 \qquad (8c)$$

More complex solids such as hexagonal crystals will have similar forms of the above equations but will have more cross terms for the greater number of independent stiffness coefficients. If the cubic is also isotropic then $c_{12} = c_{11} - 2c_{44}$ and there are only two wave velocities: longitudinal given as $V_l = \sqrt{c_{11}/\rho}$ and shear given as $V_s = \sqrt{c_{44}/\rho}$. For solids more complex than isotropic the wave velocities are direction dependent.

As with the pressure equation a finite element approximation of the elastic wave equation yields a set of linear ODE's that can be expressed in matrix format as

$$\begin{bmatrix} K_{XX} & K_{XY} & K_{XZ} \\ K_{YX} & K_{YY} & K_{YZ} \\ K_{ZX} & K_{ZY} & K_{ZZ} \end{bmatrix} \begin{Bmatrix} u_{xi} \\ u_{yi} \\ u_{zi} \end{Bmatrix} - \left[M_s \right]\left\{ \frac{\partial^2 \bar{u}_s}{\partial t^2} \right\} - \left[Q_s \right]. \qquad (9)$$

Thus there are nine distinct stiffness matrices such that

$$K_{XX} = -\int \nabla N_{xj} C \nabla N_{xi}\, dV \qquad K_{XY} = -\int \nabla N_{xj} C \nabla N_{yi}\, dV \qquad K_{XZ} = -\int \nabla N_{xj} C \nabla N_{zi}\, dV \quad (10)$$

Isotropic solids are typically characterized by Young's modulus, E, and the Poisson ratio, γ. Stiffness coefficients can be determined via the following relationships:

$$c_{11} = \frac{(1-\gamma)E}{(1+\gamma)(1-2\gamma)} \qquad (10a)$$

$$c_{12} = \frac{\gamma E}{(1+\gamma)(1-2\gamma)} \qquad (10b)$$

$$c_{44} = \frac{\gamma E}{2+2\gamma}. \qquad (10c)$$

The displacement wave equation for the fluid appears as

$$\rho_F c^2 \nabla (\nabla \cdot \vec{u}) - \rho_F \frac{\partial^2 \vec{u}}{\partial t^2} = 0 \qquad (11)$$

which, expanded, yields the three equations:

$$B\left(\frac{\partial^2 u_x}{\partial x^2} + \frac{\partial^2 u_y}{\partial x \partial y} + \frac{\partial^2 u_z}{\partial x \partial z} \right) - \rho_F \frac{\partial^2 u_x}{\partial t^2} = 0 \qquad (12a)$$

$$B\left(\frac{\partial^2 u_x}{\partial y \partial x} + \frac{\partial^2 u_y}{\partial y^2} + \frac{\partial^2 u_z}{\partial y \partial z} \right) - \rho_F \frac{\partial^2 u_y}{\partial t^2} = 0 \qquad (12b)$$

$$B\left(\frac{\partial^2 u_x}{\partial z \partial x} + \frac{\partial^2 u_y}{\partial z \partial y} + \frac{\partial^2 u_z}{\partial z^2} \right) - \rho_F \frac{\partial^2 u_z}{\partial t^2} = 0 \qquad (12c)$$

in which $B = \rho_F c^2$ is the bulk modulus for the fluid and is analogous to the elastic stiffness constants in the solid. These equations are compatible with the displacement wave equations in solids if $B = c_{11} = c_{12}$ and $c_{44} = 0$. Numerical artifacts and instabilities may arise if $c_{44} = 0$; thus, this quantity should be small but greater than 0.

Pressure can be derived from the displacement via $p = -B\nabla \cdot \vec{u}$ which in numerical form becomes

$$p = -B\left(\frac{\Delta u_x}{\Delta x} + \frac{\Delta u_y}{\Delta y} + \frac{\Delta u_z}{\Delta z} \right). \qquad (13)$$

2.3. Preprocessing of images and mesh creation

The 3D FE mesh is created from digital images (see Section 4). The desired simulation is of sound coupled to the human head via an attached transducer at different input locations. Digital images of a head can be obtained from either a CT or MRI scan. Typical scans of cadavers can be very noisy. If one looks at the individual pixel levels of these images there are many different shades of color and/or gray level values. The FE algorithm requires distinct colors or pixel values in which each value corresponds to a material type. Crisper, cleaner images were obtained by CT scanning. The scan yielded 360 2D slices. The slices were imported into a medical rendering software package known as Amira and soft tissue representing brain fluid and skin were added to recreate a replica of a human head. Transducers attached to the mastoid and forehead were also drawn in. The transducers are included in the simulation as initial results of an input signal simulated without the transducer shows the majority of the acoustic energy not being coupled into the head but radiating away from the skull. Each medium in the image is given a distinct color. This replica is in terms of acoustic properties such that the entire brain appears as a homogenous fluid-gel material. Examples of representative slices are shown below for both the original scan and the enhanced drawing. The black (royal blue) area is background and has the acoustic properties of air for the simulation.

The slices are exported from Amira as .tiff files. The .tiff files are imported into Matlab and a simple script is used to convert the colors to numbers. For instance 0 is assigned to black, 1 to green etc. The numbers for each slice are written out, in straight ASCII, to a .txt file. The .txt files are numbered in sequential order. Additional .txt files can be added at the beginning and end of the sequential list in order to have more background material above and below the skull.

The program reads in the numbers in the .txt files and each slice is assumed to have a finite thickness equal to the element length is the z direction. Thus the pixel values for the first slice become a voxel value and each of these voxels correspond to a cube element with acoustic material properties. These material properties and element dimensions are used to form the stiffness and mass matrices of the second section. Separate simulations are run for input signals with different center frequencies. As the frequency of the input signal is decreased and the wavelength increases the images are downsampled so that a distance of at least two wavelengths between the input force and the outer boundary is maintained. In Figure 1 are cross-sectional slices showing the ear canals. In Figure 2 are cross-sectional slices showing the location of the mastoid transducers. Figures 1 and 2 show different cross sectional slices of the same 3D scan. Figure 2 is a lower (caudad) slice than Figure 1. Figure 1 shows the development form the original scan to the final version. Figure 2 shows 3 different slices for corresponding reductions in frequencies. The color maps in the 2 figures are different. Intensity plots of the propagation of the signal with input at the mastoid are shown in Figure 3 for 8 kHz, 4 kHz and 1 kHz center frequencies.
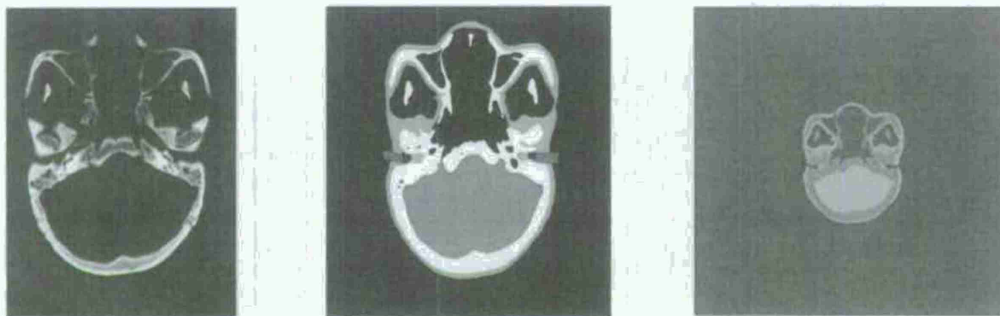

Figure 1: The original slice of a CT scan of a dry skull, the enhanced image with soft tissues and earplugs added (34 cm wide by 50.3 cm long) and the downsampled image to simulate a 4 kHz signal (68 cm wide by 100.6 cm long).

2.4. Array structure and memory conservation techniques

The program consists of 4 major sections namely the input section, the elemental matrix assembly section, the global matrix assembly section, and the time-stepping section. The input routine reads in the digital images and an input file which includes additional information about the model such as transducer location, transducer frequency, length of run and material parameters. Within the input section there are two notable

routines. One is constraint() which processes input information to determine node numbers for excitation inputs, element size, node numbers for recording time traces. The other major subroutine of the input section is 'pointer' which reads in the sequential list of digital images and assigns a 'node type' to each node based on the elements surrounding that node.
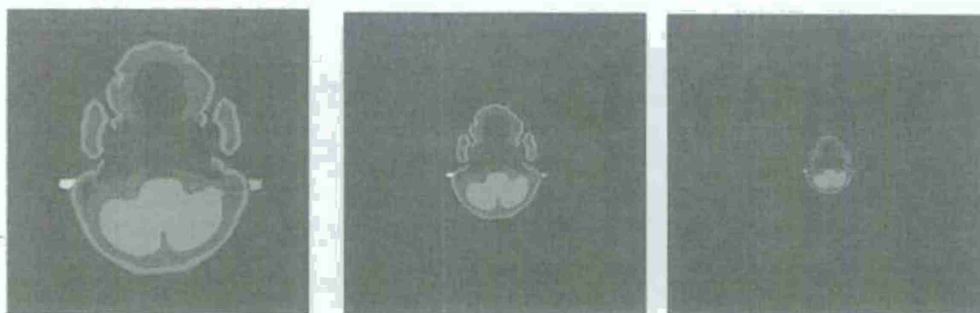

Figure 2: Slices showing the placement of the mastoid transducers. Original (a; far left) is 34 cm by 50.3 cm, downsampled by a factor of 2 (b; middle) is 68 cm by 100.6 cm, downsampled by a factor of 4 (c; far right) is 136 cm by 201.2 cm. All have 339 by 501 pixels. Each pixel is one element.
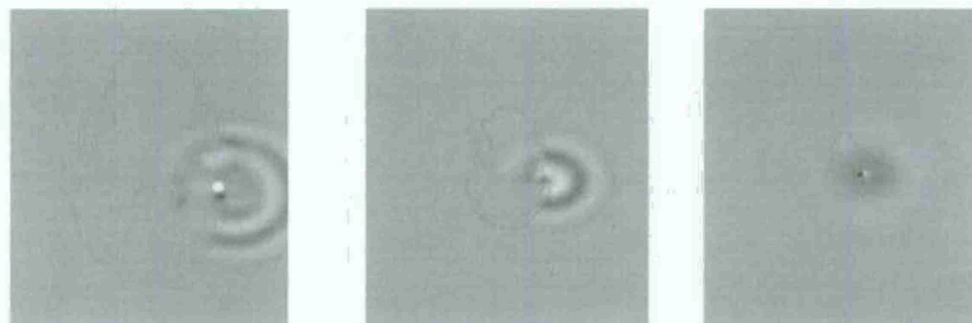

Figure 3: Intensity plots showing acoustic pressure emanating from a right mastoid transducer for 8 kHz, 4 kHz and 1 kHz.

Every element has a node at each of its 8 corners and every (non-boundary) node is surrounded by 8 elements. The pressure at each node, i, is determined by multiplying the 27 non-zero entries in the jth row of the matrix $[M]^{-1}[K_{stiff}]$. The nodes are sequentially numbered 0 through N-1 starting with the lower left node of the bottom slice. The rows are not unique. For instance all the black or background nodes will have identical values for the 27 entries. The same is true for the other color nodes. Interface nodes between colors may also be repeated. There are 8 elements (or pixels) surrounding each node. If an interface node between two materials has the same pattern of elements around it as another interface node then these 2 nodes are of the same type. There is a global integer array, of length N, known as NodeType and for each node, i, NodeType[i] identifies the

type of node. An array known as PixType identifies the type of pixel or element. Node i is surrounded by PixType[i-1], PixType[i], PixType[i+NX1-1], PixType[i+NX1], PixType[i+NLAY-1],PixType[i+NLAY], PixType[i+NLAY+NX1-1] and PixType[i+NLAY+NX1] or elements A, B, C, D, E, F, G and H in Figure 4. Note that NX1 is the number of nodes in a row in the x direction and NLAY is equal to the number of nodes in a slice or NLAY=NX1XNY1.
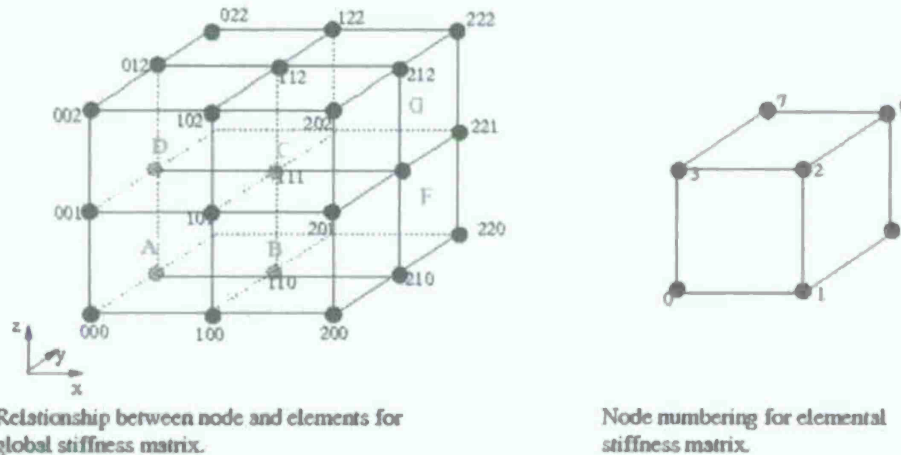
Relationship between node and elements for global stiffness matrix.

Node numbering for elemental stiffness matrix.

Figure 4. Node Elements in the Computational Model

The 27 entries of a $[K_{stiff}]$ row are stored in a 3 x 3 x 3 array known as the global stiffness array UNKF[i][j][k][l] (or UNKF_AB[i][j][k][l] in which A and B are X, Y, Z for the displacement-based code). The fourth dimension references the node type. For instance all the background nodes will have NodeType[i]=4 and therefore UNKF[i][j][k][4] will store the stiffness array entries for node type 4. The number of different node types depends on the number of different materials plus however many unique interface nodes exist. This value is stored in a variable NumUniqueNodes and is always an integer several orders of magnitude less than 64 million.

The global stiffness array(s) is assembled, for each node type, in the routine GlobMatAssemb. The array is assembled from the elemental stiffness array, EKF[i][j], which is formed in the routine ElemMatAssemb. The elemental stiffness array is an 8 x 8 matrix and relates each local node in the element to every other local node. See Figure 4 for local node numbering. There is a third dimension in EKF that references the material type of that element. Note that unlike the global stiffness matrix for the nodes, EKF will only have the number of types equal to the number of materials in the model, usually 3 or 4, since elements are not split across interfaces. The GlobMatAssemb routine forms the stiffness matrix by mapping EKF from the local node into UNKF for the global node type. For instance referring to Figure 4 UNKF[0][0][0] is equal to EKF[6][0] of element A while UNKF[1][0][0] is equal to EKF[6][1] of A plus EKF[7][0] of B. An array known as IntFaceNodeType maps the element type of EKF to the node type for UNKF.

The same general principles are used to assemble the mass matrix array but it is much easier since the mass matrix is diagonal according to a well established FE mass lumping technique.

2.5. Parallelization using Message Passing Interface (MPI)

The current trend in supercomputer architecture is towards distributed memory machines or clusters in which larger autonomous processors with individual memory banks are linked together through a high speed communications port. These machines are easier, hence cheaper, to build.

In order to take advantage of availability and speed of distributed memory machines the algorithm is adapted to these clusters using MPI routines. In a shared memory architecture there are many small processors but they all access the same core memory and there is a main interface node that controls all the other processors, whereas in a distributed memory machine each processor has its own memory bank and all the processors work independently of each other. Therefore, there needs to be communication between the processors. Programming in MPI on clusters requires a slightly different mindset because the program will be launched on all the processors when it is executed. Thus when a program is running on a 10 node cluster, there will actually be 10 versions of that program running and 10 values of all the variables defined in that program. It is possible to limit statements and variables to an individual processor as there is a variable known as my_rank which is equal to the processor or node number. Note that processors in clusters are also referred to as nodes and should not be confused with the nodes in the finite element mesh. Thus to define a variable N=100 on node 5 a program could have the statement if(my_rank==5) N=100. Without the 'if' statement there would be 10 variables equal to 100 on all the nodes.

The current program is adapted to clusters by assigning one slice, in the digital image set, per processor. Thus in the current example there are 400 slices with 400 x 400 nodes each so the MPI code would be launched on 400 processors. The slice number will correspond to the processor number. Within the TimeStepAlg routine the inner loop will step through 400 x 400 = 160,000 nodes rather than 64 million nodes. When it executes 400 processors will step through 160,000 nodes rather than one master processor stepping through 64 million nodes. Naturally each processor will need to know also the pressures for the slices immediately above and below it or the z+1 and z-1 slice. This communication is done with MPI_Send and MPI_Recv commands. At every time step before the pressures are computed a set of MPI_Send and MPI_Recv commands are given so that the processor for every slice has the information from the adjoining slice. Arrays UFFr and UFBk are length 160,000 and store the pressure values for the z+1 and z-1 slices respectively. It is important to have MPI_Barrier commands before and after each time-step so that one processor does not get ahead of (or behind) the others.

In addition to the routines updating the pressure, the Pointer subroutine also requires MPI commands. The my_rank variable is used so that each processor reads in only one slice. As with most of the variables the NodeType array will be defined on all

the processors and will have a length of 160,000. In order for the routine to determine what type a node is the pixel or element types from the adjoining slice must be used. Therefore within the pointer subroutine the pixel type information from the adjoining z-1 slice is sent to the z processor and the z processor uses this information to determine node type.

There is no message passing among the nodes in the ElemMatAssemb and GlobMatAssemb routines. Each processor will have its own value for NumUniqueNodes and its own set of EKF and UNKF matrices. This means there will be duplication of these matrices since many of the node types on one processor will be the same as on another. This tradeoff in memory conservation is justified by the ease and simplicity of having each processor use its own set of matrices when updating the pressures at nodes in its slice.

2.6. Computational model results

Simulations of experimental tests, in which transducer inputs are located at different head locations and behavioral assessment of sound is recorded, are used to assess the efficacy of the numerical model. Acoustic pressure level measurements in the ear (auditory canal and cochlea) and back of the head for transducers at the right mastoid (Table 1) and forehead (Table 2) are tabulated. The flexibility of numerical simulations allows one to determine pressure levels at any point in the model area. For these results the earplugs were turned off by setting their material parameters equal to those of air. Measurement points are in the air pathways (auditory canal) of both ear canals and in the bone connected to the inner ear (cochlea) as well as in the bone at the back of the skull. The fact that resulting pressure is generally higher in the air pathway (auditory canal) indicates that not all the input signal is being coupled to the skull and some energy is being conducted via the background air as is also indicated by Figure 3. More complete coupling is being achieved with the experimental setup. It is possible to determine the error due to air conducted energy by modeling the transducer without the head target and subtracting the total incident field from the total field.

2.7. Three-dimensional simulation results of the occlusion effect

The occlusion effect was modeled numerically and in three dimensions by giving the earplugs in Figure 14 (Section 4) a sound speed of 1878 m/s and a density of 1200 kg/m^3. Plots of the pressure measured in the right ear canals for the right mastoid mounted transducer centered at 3 kHz are shown in Figure 5. Note that there is considerably more ringing in the occluded ear and the magnitude of this ringing is frequency dependent. Results showing the peak of the ringing to the input are displayed in Table 3. The pressure is higher in the occluded ear than in the unoccluded for all frequencies. For the occluded ear the pressure is higher at 1 kHz and 4 kHz than at 2 and 3 kHz.

Table 1: Acoustic pressure measurements as a function of frequency in the ears at the specified locations for transducer attached to the right mastoid. The pressure level (in dB) is that recorded at the indicated site (auditory canal or cochlea) relative to the pressure level just under the transducer in the skin.

	4 kHz	3 kHz	2 kHz	1.5 kHz	1 kHz
Right auditory canal	3.1 dB	-1.0 dB	-5.7 dB	-21 dB	-26 dB
Right cochlea	-4.5 dB	-4.0 dB	-3.4 dB	-18.5 dB	-19.8 dB
Left auditory canal	-52 dB	-51.6 dB	-55.6 dB	-70.5 dB	-73.7 dB
Left cochlea	-56 dB	-56 dB	-53 dB	-22.5 dB	-32 dB
Back of head	-77 dB	-71.6 dB	-67 dB	-75 dB	-71 dB

Table 2: Acoustic pressure measurements as a function of frequency in the ears at the specified locations for transducer attached to the forehead. The pressure level (in dB) is that recorded at the indicated site (auditory canal or cochlea) relative to the pressure level just under the transducer in the skin.

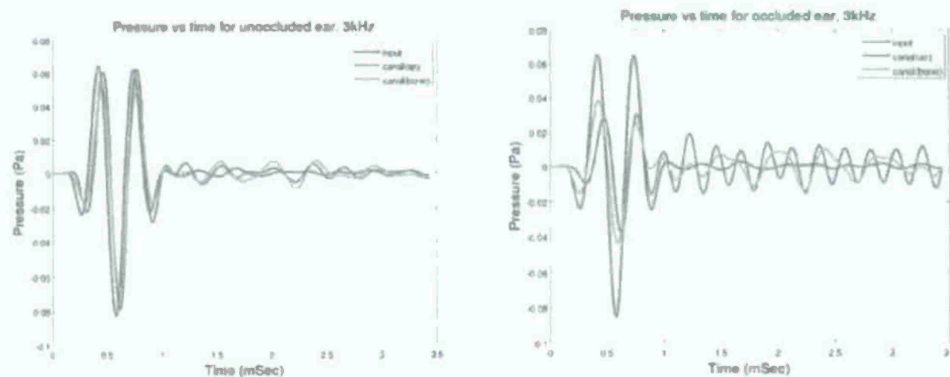|	4 kHz	3 kHz	2 kHz	1.5 kHz	1 kHz
Right auditory canal	-52 dB	-37.4 dB	-54 dB	-66 dB	-76 dB
Right cochlea	-59 dB	-41.6 dB	-55 dB	-80 dB	-70 dB
Left auditory canal	-60 dB	-35.6 dB	-54 dB	-76 dB	-79 dB
Left cochlea	-70 dB	-48.8 dB	-66 dB	-60 dB	-79 dB
Back of head	-98 dB	-74.8 dB	-80 dB	-105 dB	-98 dB

Figure 5. Plots of pressure versus time in the ear canal and ear canal bone for the unoccluded (left) and occluded (right) ear. Input signal is blue, pressure in canal air passage is green and pressure in canal bone is red.

Table 3. Simulation results, in dB, of pressure in the ear canal air passage-way as a function of frequency for the occluded and unoccluded ear.

	1 kHz	2 kHz	3 kHz	4 kHz
unoccluded	-19dB	-19dB	-24db	-22dB
occluded	-9.5dB	-11dB	-15dB	-5dB

3. CONCENTRIC SPHERE FINITE ELEMENT MODEL

Like many numerical methods, it is possible to have divergent solutions. It is therefore important to validate the model with geometries that have analytical solutions. One such geometry is that of two concentric fluid spheres. One can approximate the human head as two concentric spheres where the outer sphere has the bulk fluid properties of bone (in this case neglecting the presence of shear waves) and the inner sphere has the properties of water (McNew et al., 2009).

The choice to use concentric spheres provides a simple starting point for verification, especially because of the availability of a closed form solution. Verification has been focused on the comparison of specific spatial points of FEM fluid and solid against the fluid concentric sphere closed form solution. These points have in addition been studied in an experimental setting (recorded using hydrophones, microphones and accelerometers). Work is under way to verify the model results against these experimental results.

The computed ANSYS FEM models were based on a 3D tetrahedral mesh with spherical boundaries. This mesh is a requirement by ANSYS to provide infinite boundaries (open air). Interpolation inside of the tetrahedra was used to find the pressure values for specific spatial locations. The Visualization Toolkit (VTK) open source library was used to facilitate this task.

The ANSYS model was first exported into a file format compatible with VTK. It was then read and analyzed using the built in reader and probe filter in VTK. Probe filter finds the interpolated scalar quantities at specified locations or at the points of a new mesh. Pressure waves were exported into a format readable by Matlab, to allow for quick computation and renderings.

The same incident signal was used both in the closed form solution and in the FEM models. This signal is a raised cosine at center frequency of 500 Hz (Figure 6).

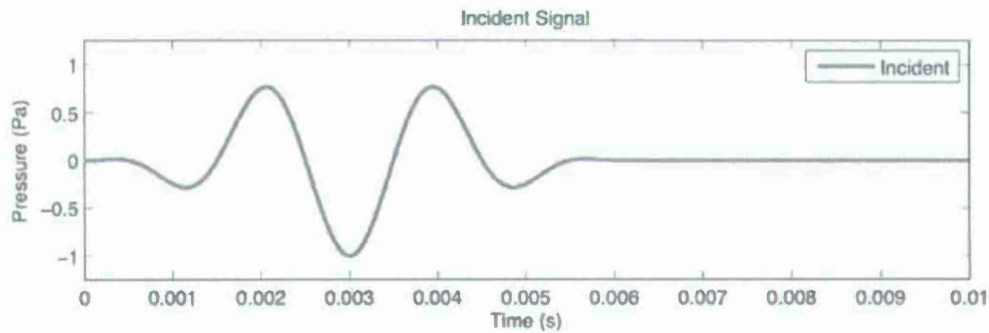$$y(t) = \frac{1}{2}\left(1 - \cos\left(\frac{\omega t}{3}\right)\right)\cos(\omega t). \tag{14}$$

Figure 6. Incident pressure wave.

The time signals shown correspond to the points marked in Figure 7. Time pressure signals superimposed in Figures 8 through 10 show pictorially the level of agreement between the FEM models and the closed form solution. The plots show good agreement between the different solutions with amplitude differences between solid and fluid simulations, and as the wave propagates into the concentric spheres, a period difference begins to appear. Figure 8 shows the pressure wave at an early stage, still traveling in air. Figure 9 shows the wave at the center of the spheres. The period difference observed at the center is $\Delta T = 0.1$ ms or a shift in center frequency of $\Delta f = 37$ Hz.
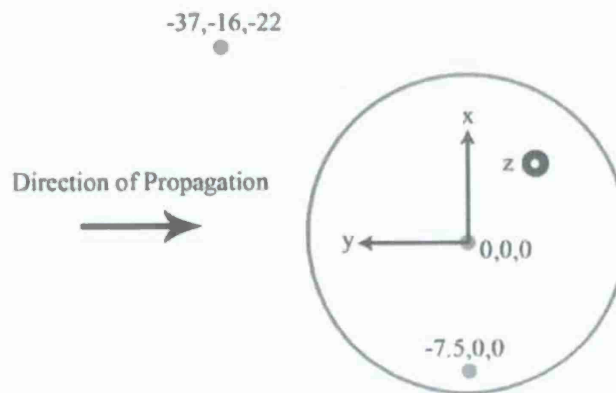
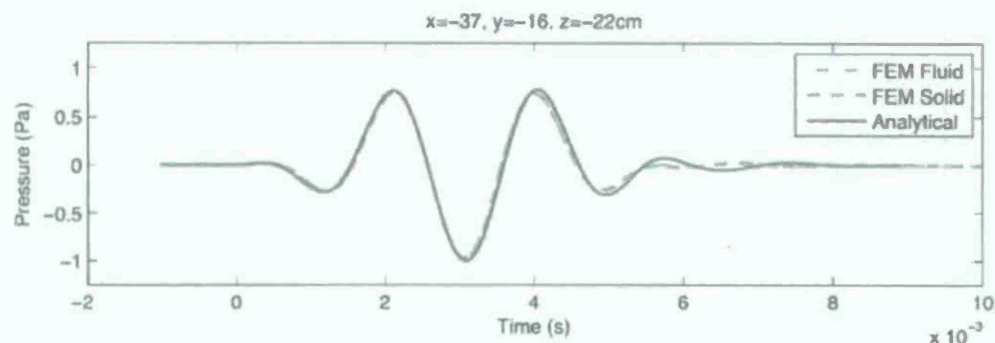Figure 7. Points at which pressure was computed (in green).

Figure 8. Pressure at reference microphone placed outside of the sphere nearest to the acoustic source.
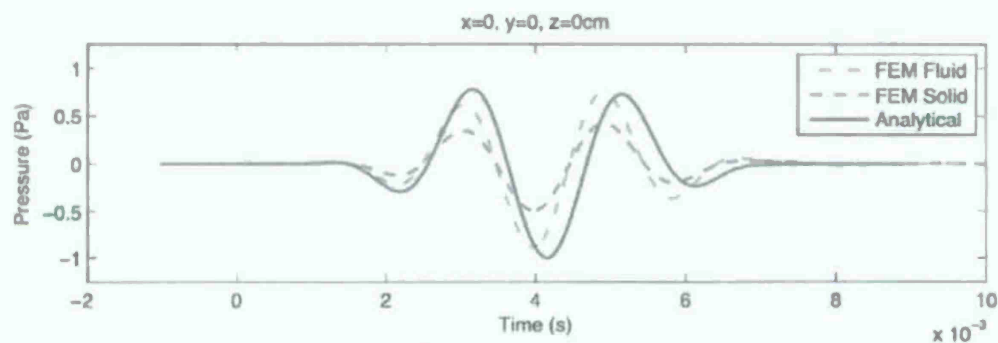

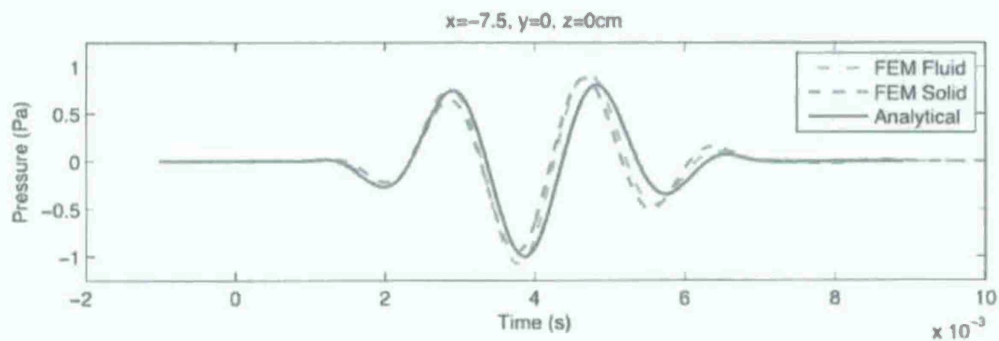Figure 9. Pressure at point at center of concentric spheres.

Figure 10. Pressure near edge of inner sphere.

3.1. Comments

A finite element model was formulated for simulating the acoustic wave propagation into concentric spheres. This model was verified against the closed form solution of the plane wave propagation into concentric fluid spheres. Good agreement is

seen between the analytical and numerical solutions. The main artifact observed in the numerical solution is a small shift in pulse length and center frequency.

The cause of this numerical inconsistency can be related to the mesh size (element edge length per wavelength). Figures 8, 9, and 10 support the above statement by showing how the error becomes more prominent as the plane wave propagates in the domain. The current computational limitations make it difficult to obtain finer meshes (shorter element edges) for the same domain size and medium acoustic properties, however examining smaller problems both in the analytical solution and FEM solution could be a feasible compromise.

4. COMPUTED TOMOGRAPHY (CT) IMAGE SEGMENTATION

To obtain a 3D segmented volume from Computed Tomography (CT) images of a cadaver, the software package Amira was used. DICOM (Digital Imaging and Communications in Medicine) slices were obtained and imported into Amira. Segmentation was performed by means of data thresholding (by brightness level) and also by manual volume selection. Amira allows for complex manipulations of the volume to be segmented, such as the translations, rotations, growth, addition, and removal of material. These functions became essential at eliminating artifacts from the CT images.

The resulting volume (Figure 11) contains only information about the materials of interest present in the object (artifacts have been removed). Moreover, each material is labeled with a unique identifier (in this case, a unique color). This allows for quick manipulation at a later time.
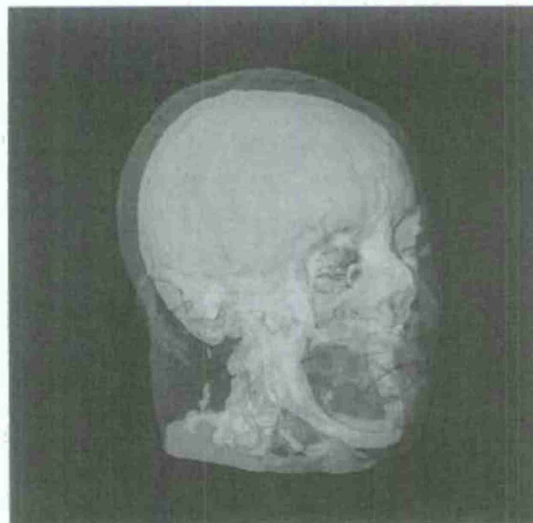

Figure 11. Segmented volume.

Once the necessary manipulations have been performed, different materials are segmented into layers. These layers contain non-overlapping material (no piece of material can be in two or more layers). Figure 12 shows orthogonal CT cross sections with overlaid material boundaries, and a 3-D rendering of the segmented volume.
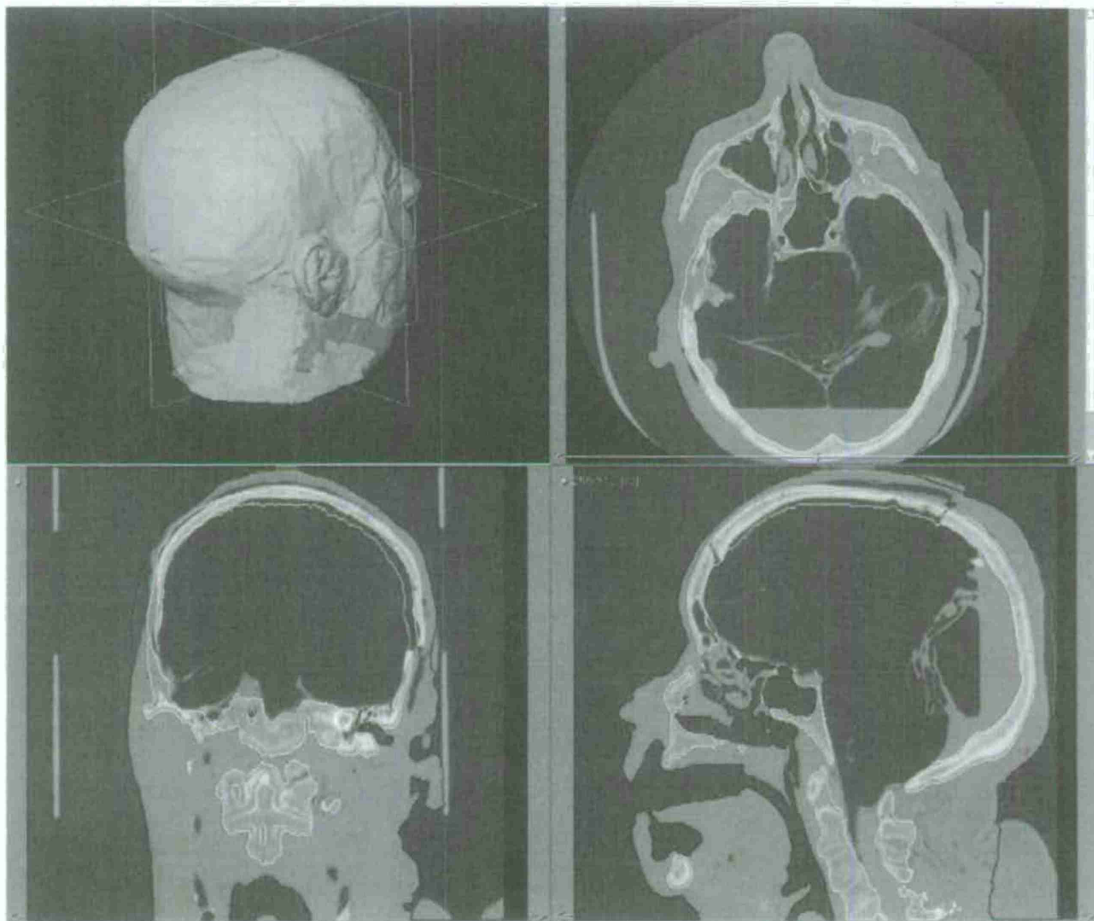

Figure 12. Segmentation with Amira. Top left: Segmented volume (transparency effect added.) Other three panels: Orthogonal CT cross sections with color lines showing the boundaries of each layer.

Each of these layers is assigned a color (Figure 13), which is used for display, and in our case as the input to a routine that assigns acoustic properties to the skin, bone, and brain.
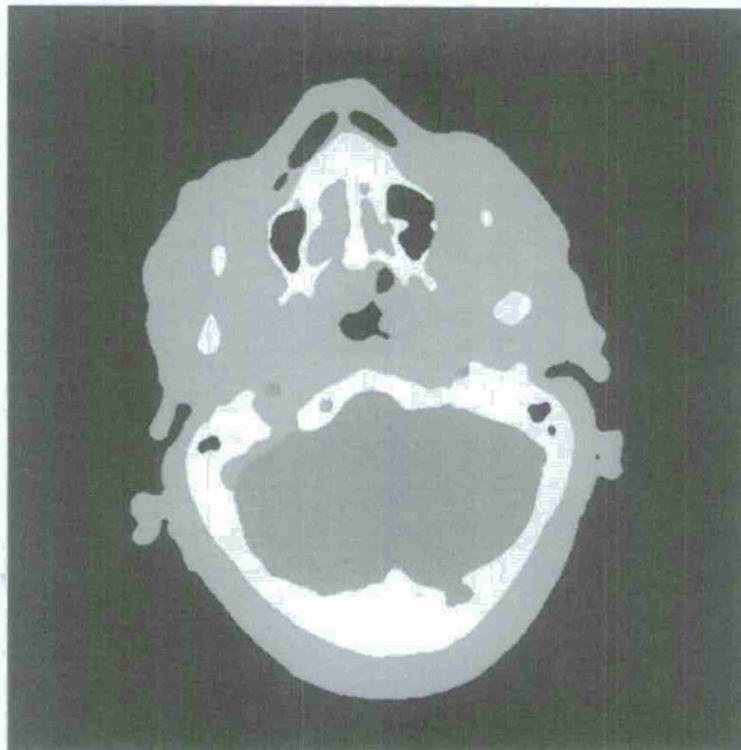
Figure 13. Segmented slice from CT scan of human head human head. Black: air, red: skin, white: bone, green: brain.

Images such as Figures 12 and 13 are the input to modeling software that is able to assign acoustic properties, and signal sources, to any pixel of an image. The addition of earplugs and bone conductors to the model meant "drawing" them into the segmented volume in Amira.

Bone conductors were modeled to be cylindrical in shape. They are composed of an active region, were the signal will be provided, and a body, representing the casing of the mechanical parts. A perfect coupling between the active region and the skin of the model was assumed.

Figure 14 shows a segmented slice of a dry skull CT-scan (with grown in skin). In this model, Amira was used to draw in ear plugs (blue) and bone conductors (purple and teal). A brighter color was used to represent the active area (that generate sound) for the each bone conductor. Ear plugs were modeled to be cylindrical as well. They have a perfect fit with the ear canal.
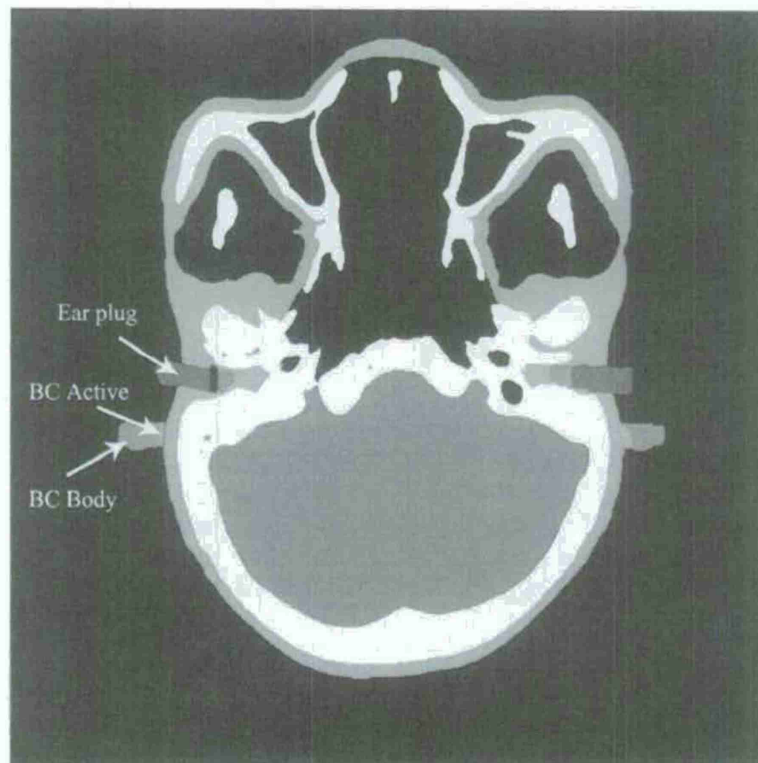
Figure 14. Segmented slice from CT scan of dry skull with grown in skin.

5. ACOUSTIC RAY TRACING

Acoustic ray tracing is a technique to visualize the direction of propagation of an acoustic wave as it travels through a medium. The idea of applying ray tracing to acoustic problems has also been studied as a component of this grant (McNew, 2008; Bellina, 2009). Herewith is proposed, a new ray tracing approach based on the notion of isosurfaces is presented. It is first developed for a uniform medium, and a plane wave is used as the input signal. The second development is for an oblique incident plane wave on a planar interface between two media with different sound speeds. The computed angles are compared to the predicted angles by Snell's law. Ray tracing is also applied to the concentric sphere case.

5.1. Wavefront reconstruction

The first step to ray tracing from a scalar field is to reconstruct wavefronts. Pierce (1989) describes wavefronts as surfaces in which a given feature of a signal arrives at the same time. Alternatively, in the frequency domain, wavefronts are defined as the surfaces of equal phase.

Finding wavefronts: Another way of phrasing Pierce's definition is to say that we want to find the time delays between an incident signal $p_{inc}(t)$, and each point of the volume $p_{x,y,z}(t)$ in question, where $p_{x,y,z}(t)$ is the time pressure signal obtained by picking point (x,y,z). We can of course perform this operation by means of cross-correlation:

$$p_{inc}(t) * p_{x,y,z}(t) = \int_{-\infty}^{\infty} p_{inc}(\tau) p_{x,y,z}(t+\tau) d\tau . \tag{15}$$

Alternatively, we can perform the same operation by finding the cross-correlation in the frequency domain, and then applying the inverse Fourier transform:

$$F^{-1}\left\{ F\left\{ p_{inc}(t) \right\}^* F\left\{ p_{x,y,z}(t) \right\} \right\}, \tag{16}$$

where F is the Fourier transform and * is the complex conjugate. The later expression makes more efficient use of computational resources because the Fourier transform of the incident signal needs only to be obtained once.

Once the correlated signal is computed (p_{corr}), the lag at the maximum point of correlation is found by taking the Hilbert transform of p_{corr}, and then computing the maximum value of its magnitude:

$$\max\left(\left\| \text{Hilbert}\left(p_{corr}\right)\right\|\right). \tag{17}$$

Matlab's command *max* will return both the maximum value, and the lag. The returned lag is then stored in a 3D matrix with the same number of points as the original volume. Therefore the steps are:

1. Obtain a time dependent pressure scalar field in 3D volume.
2. Obtain an incident waveform.
3. Take the 1D time correlation for each point of the volume with the incident signal.
4. Find the lag corresponding to the arrival of the incident waveform at that point.
5. Store lags in an arrival time volume.

A resulting arrival time volume (Figure 15) contains the time for each point when the incident signal arrived.
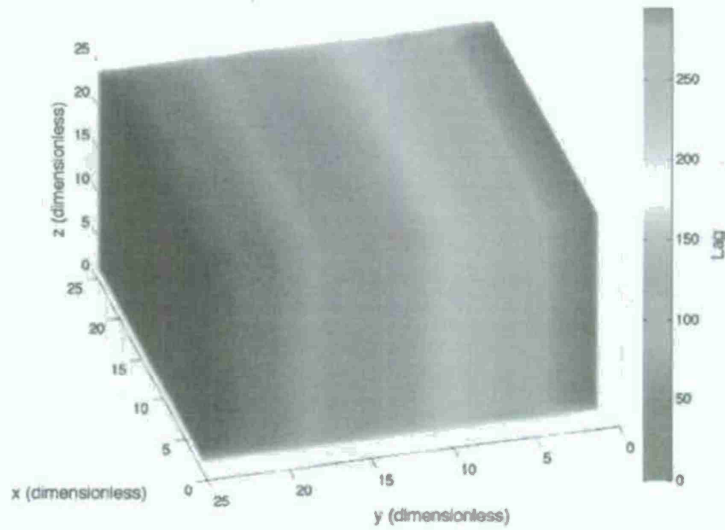
Figure 15. Arrival times volume from a plane wave traveling in a uniform medium.

Finding wavefronts: From an arrival times volume we can define wavefronts as isosurfaces, that is surfaces of equal lag (Figure 16). This is done in Matlab simply by the *isosurface* command, which returns a mesh of faces and vertices corresponding to elements on that surface.
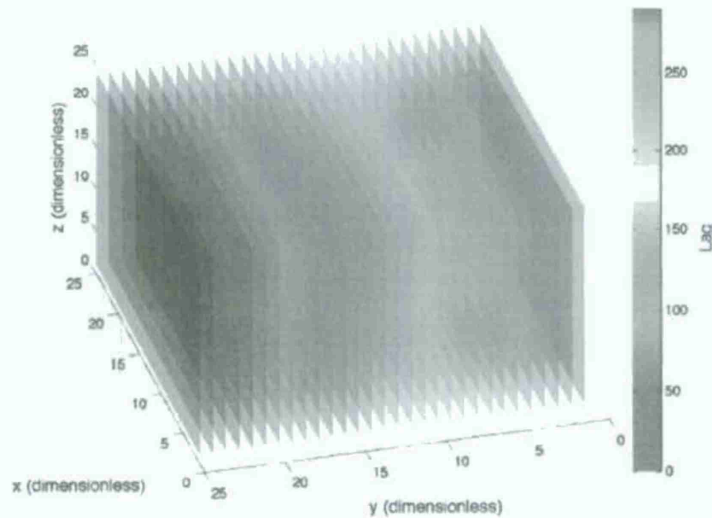

Figure 16. Reconstructed wavefronts from a plane wave traveling in a uniform medium.

Ray Tracing: Using the previously generated wavefronts, the next step is to draw the path that a signal will take while traveling in the medium. The resulting path is a *ray*. The general procedure for obtaining rays from wavefronts is as follows:

1. Obtain current t_1 and next isosurface t_2.
2. Find normals at each vertex of t_1.
3. Compute the intersection of each normal with the planes containing each face of isosurface t_2.
4. Find the face that contains the intersected point.
5. Set the intersected points in isosurface t_2 as the new starting point of the algorithm (i.e., t_1).
6. Repeat.

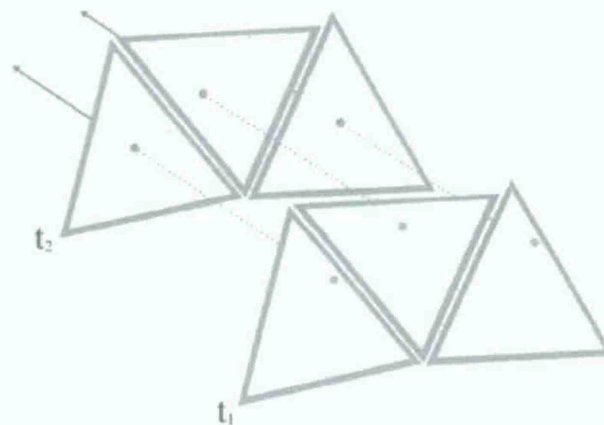Figure 17 shows a snapshot of the algorithm between two isosurfaces.

Figure 17. Triangles from two isosurfaces (t_1 and t_2) are depicted as rays normal to t_1 (starting on the red dots) intersect inside the triangles on t_2 (ending on the green dots). The process is repeated for the next isosurface.

The collection of rays found using the algorithm outlined above is drawn together in a volume to show the direction of wave propagation. Figure 18 shows the rays found in a uniform medium. Notice that all of the rays form a straight line along the direction of propagation. This is both because the medium is uniform and a plane wave stimulus is used.
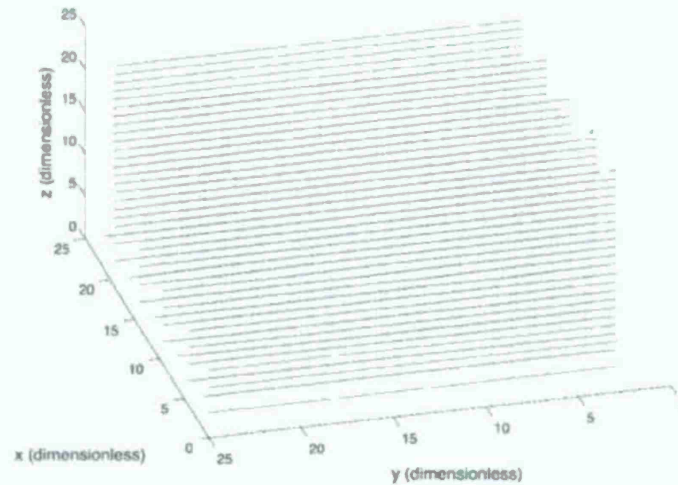
Figure 18. Rays from a plane wave traveling in a uniform medium.

5.2. Plane wave at oblique incidence on a planar interface

Results were obtained on a domain that was split in two equal rectangles. The first half had sound speed c_1, and the other c_2. Other physical properties were kept constant and are not included in this study. A plane wave with oblique incidence (not perpendicular to the interface) was introduced from one end (Figure 19).
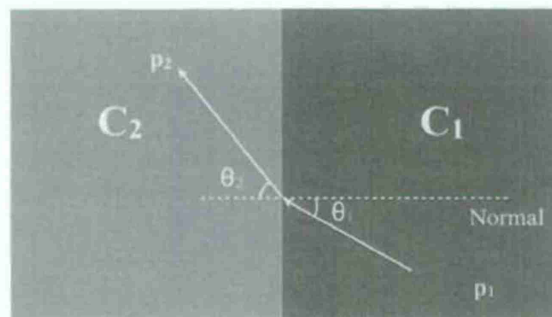

Figure 19. Cross-section of domain showing two domains (green and blue) with different sound speeds, the incident and transmitted plane waves, and their respective angles with respect to the normal of the interface.

This problem is governed by the ratio of sound speeds at the interface, that is, by Snell's law:

$$\frac{c_2}{c_1} = \frac{\text{Sin}(\theta_2)}{\text{Sin}(\theta_1)}, \tag{18}$$

where θ_1 and θ_2 are the incident and transmission angles, respectively. A pressure field was computed by implementing the following equations:

$$p_1 = e^{j(k_1 x \text{Cos}(\theta_1) + k_1 y \text{Sin}(\theta_1))} \tag{19}$$

$$p_2 = e^{j(k_2 x \text{Cos}(\theta_2) + k_2 y \text{Sin}(\theta_2))}, \tag{20}$$

where k_1 and k_2 are the wave numbers, and x and y are the Cartesian spatial coordinates. Given an incident angle θ_1, we can use Equation 18 to calculate θ_2:

$$\theta_2 = \text{Sin}^{-1}\left(\frac{c_2}{c_1}\text{Sin}(\theta_1)\right), \tag{21}$$

Pressure fields were obtained from Equations 19 and 20 as a function of sound speeds and incident angle. Arrival time volumes and wavefronts were reconstructed from these pressure fields for a variety of sound speed ratios and angles of incidence.

In contrast with the uniform field arrival time volume (Figure 15) and wavefronts (Figure 16), the arrival time volumes and wavefronts obtained here show a line of diffraction, caused by a change in sound speed. Figure 20 shows such an arrival time volume, Figure 21 shows the resulting wavefronts, and Figure 22 shows the rays traced for a domain with $c_1 = 300$ m/s, $c_2 = 330$ m/s, and an incident angle $\theta_1 = 45°$. Line x = 25 in these plots shows the interface between the two halves.

5.3. Plane wave at oblique incidence on a planar interface: Results

Ray tracing simulations were run for different sound speed contrast ratios and angles of incidence. The incident angles were chosen to be less than the critical angle for each sound speed ratio. The critical angle is given by Snell's law when the transmission angle θ_2 is 90°:

$$\theta_c = \text{Sin}^{-1}\left(\frac{c_1}{c_2}\right). \tag{22}$$

Each arrival time volume was a 50x50x10 3D grid. The predicted angle and computed (mean) angle were recorded for each case and are presented in Table 4. There was full agreement when the angle of incidence was 0°, as expected. Small differences are observed between the predicted and computed values.
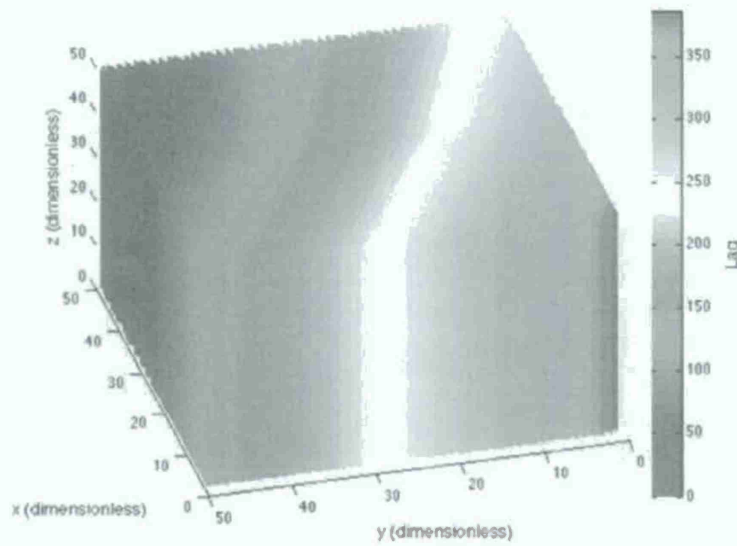
Figure 20. Arrival time volume for the plane wave with oblique incidence on a planar interface case.
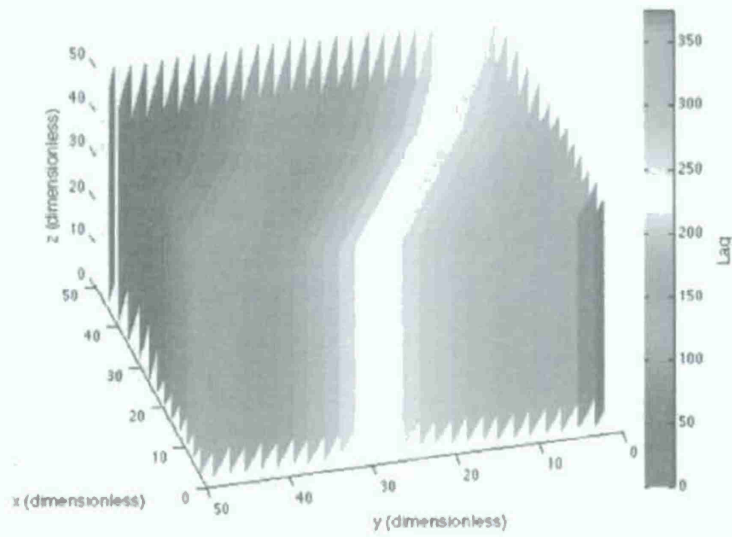

Figure 21. Reconstructed wavefronts from the oblique incidence on a planar interface case.
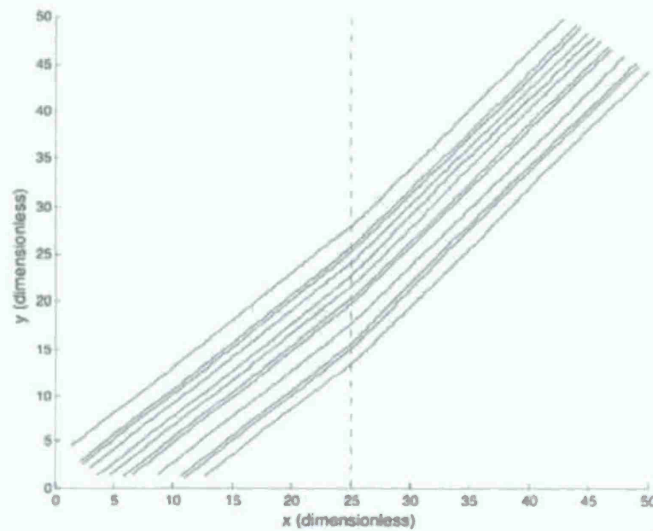
Figure 22. Rays traced from the oblique incidence on a planar interface case (top view). The dashed line shows the interface between the two domains.

Table 4. Comparison of predicted incident and transmission angles (θ_1 and θ_2) and the computed angles ($\tilde{\theta}_1$ and $\tilde{\theta}_2$) by ray tracing for three sound speed contrast ratios. The computed values shown are the mean angles found across ray segments. E_1 and E_2 are the relative errors (represented as percent) between the predicted and computed angles, $E_i = \left| \tilde{\theta}_i - \theta_i \right| / \theta_i$.

c_1 (m/s)	c_2 (m/s)	θ_1	$\tilde{\theta}_1$	θ_2	$\tilde{\theta}_2$	E_1	E_2
300	310	0°	0°	0°	0°	0%	0%
		10°	10.12°	10.34°	10.33°	1.2%	0.1%
		30°	30.05°	31.11°	31.10°	0.17%	0.03%
		45°	44.97°	46.94°	46.88°	0.07%	0.34%
		60°	59.97°	63.49°	63.19°	0.05%	0.47%
300	320	0°	0°	0°	0°	0%	0%
		10°	10.17°	10.67°	10.70°	1.7%	0.28%
		30°	30.11°	32.23°	32.22°	0.37%	0.03%
		45°	44.91°	48.96°	48.39°	0.2%	1.16%
		60°	59.81°	67.48°	63.19°	0.32%	5.93%
300	330	0°	0°	0°	0°	0%	0%
		10°	10.13°	11.01°	11.03°	1.3%	0.18%
		30°	30.06°	33.37°	33.20°	0.2%	0.51%
		45°	44.93°	51.06°	50.94°	0.16%	0.24%
		60°	59.76°	72.29°	72.09°	0.4%	0.28%

The results in Table 4 suggest that the ray tracing algorithm is accurately predicting angles of incidence and transmission. The error levels are for the most part less than 0.5%.

An interesting trend is that for each of the $\theta_1 = 10°$ runs, the error was close to 1.5% for the incident angle. Another seemingly different error estimate is found for the transmission angle for the 300/310 m/s sound speed ratio and 60° degrees incidence run. In that case, the error was 5.93%. It is believed that the starting conditions, at the ray tracing level, are responsible for these differences. Ray tracing starts with the choice of the first isosurface, and then a number of isosurfaces follow. This choice is not the same for each of the runs, hence the difference in errors between incident angles. In addition to this observation, the algorithm does not use all of the isosurfaces found. Instead, a down sampling operator is used to choose isosurfaces that at multiples of a number (i.e. every two isosurfaces, every four, etc). This is done in order to control computation time.

5.4. Wavefront reconstruction applied to a fluid sphere

A low contrast simulation was run to test the ray tracing method on a fluid sphere submerged in a uniform medium. A 3D pressure field was obtained from the analytical wave equation solution. The model parameters for the fluid sphere are listed in Table 5.

Table 5. Physical properties of concentric fluid spheres simulation.

Medium	Density (kg/m^3)	Sound Speed (m/s)	Radius (cm)
Outside of Sphere	1	300	
Sphere	1	400	9

Figures 23 and 24 show a top view and a perspective view, respectively, of the fluid sphere ray traces. Figure 23 shows that rays start with a uniform distribution at the source of acoustic pressure ($y = 50$). As the wave propagates towards the sphere, rays in its vicinity focus into it, increasing the concentration of rays at the center of the image. Once the rays leave the sphere, their distribution is no longer uniform. It is evident at $y = 0$ that there is a pattern in ray concentration for the rays that intersected the sphere.

Because this is a 3D model, the acoustic source is a plane wave, and the scatterer is a sphere, we would expect that the focusing effect would happen symmetrically in every direction. Figure 24 is a perspective view of the same simulation showing the symmetry described above.
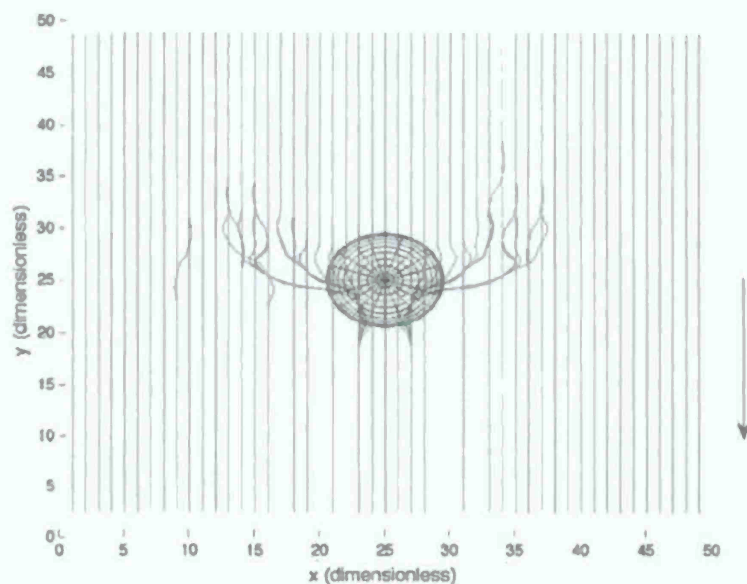
Figure 23. (Top view) Rays obtained from the analytical solution for a water sphere (18 cm diameter, 5 mm thickness) in air. Incident signal was a raised cosine pulse at 500 Hz.
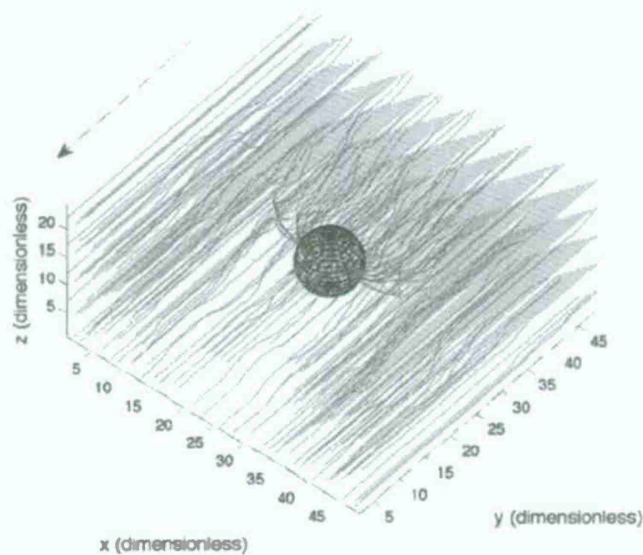

Figure 24. (Perspective view) Rays obtained from the analytical solution for a water sphere (18 cm diameter, 5 mm thickness) in air. Incident signal was a raised cosine pulse at 500 Hz.

5.5. Comments

A ray tracing method was developed to visualize the acoustic wave propagation pathways from a scalar pressure field. This technique is based on the notion of equal pressure wavefronts, or isosurfaces, obtained from an arrival time volume.

To find wavefronts from a scalar field, time correlation is performed at each point of the volume between the incident signal and the total acoustic pressure at that point. The maximum lag found in this operation becomes the arrival time value for that point in space. Having found the wavefronts, rays are traced by finding the intersection of normals from one wavefront onto another wavefront repeatedly.

Verification of the ray tracing technique involves generating pressure fields with known wavefronts, and therefore with known ray directions. A pressure field for a plane wave incident onto a uniform field was found and the ray tracing technique was used successfully, finding the predicted wave propagation direction. A plane wave with oblique incidence on a planar interface between two media with different sound speeds was also simulated, and the rays computed were verified against those predicted by Snell's law, finding good agreement between them.

6. HUMAN SUBJECT TESTING

Human subject testing was conducted to acquire and to apply empirical data from human listeners stimulated with bone conduction signals to develop and verify a functional model of bone conduction propagation pathways in the human skull. Specifically, the aims of the studies were (1) to evaluate evidence of occlusion effects from bone conduction hearing as a function of stimulus location and frequency in open versus closed ear canals, and (2) to determine the relation, if any, between static force applied to the bone-conduction oscillator and hearing sensitivity (thresholds) as a function of oscillator location and stimulus frequency in open ear canals.

All participants were between 18-30 years of age with normal hearing, no structural abnormalities of the head or neck, no history of ear surgery, otologic or neurologic disease, or head trauma.

6.1. Evidence of occlusion effects in bone conduction hearing

Purpose: Evidence of bone-conducted sound pathways through the skull have been explored with growth of loudness tests, auditory brainstem response and otoacoustic emissions; however a comprehensive understanding of these pathways has not been achieved. Less is known about the usefulness of behavioral thresholds, sound pressure levels in the ear canal, and the auditory steady-state response (ASSR), as a function of ear canal occlusion in understanding propagation pathways of bone-conducted signals for

different oscillator placements. Data for bone-conduction hearing are critical to test numerical simulation results.

Procedure: Behavioral thresholds (determined in 1-dB steps) and RMS SPL measures for bone conduction stimuli at 40 dB HL were acquired with ear canals open and closed in four young adults. Ear canal status (open vs. closed) and bone oscillator placement (forehead vs. right mastoid) were evaluated across the frequency range of 250 to 4000 Hz. In addition, ASSR measures were obtained across repeated test sessions in a single subject for bone-conduction stimuli presented at 40 dB HL at four frequencies: 500 Hz, 1000 Hz, 2000 Hz, and 4000 Hz at two placement locations: forehead and mastoid.

Result Summary: Thresholds were less sensitive in the open condition compared to the occluded condition from 250 Hz to 2000 Hz. In addition, the RMS in the ear canal was higher in the occluded conditions below 2000 Hz. This trend in hearing sensitivity and RMS values were reversed above 2000 Hz. ASSR results, a suprathreshold measure, were also lower (more sensitive) in the occluded condition across frequencies. The ASSR results were acquired in a single-subject across multiple repeated tests sessions. Sample results, shown in Figures 25 and 26, provide evidence of the occlusion effect for both behavioral and physiologic measures as a function of oscillator placement. Given that the ASSR was consistent with the behavioral results and did not offer additional information for modeling of bone-conduction propagation pathways in the human skull, further ASSR testing was not indicated for the current project.

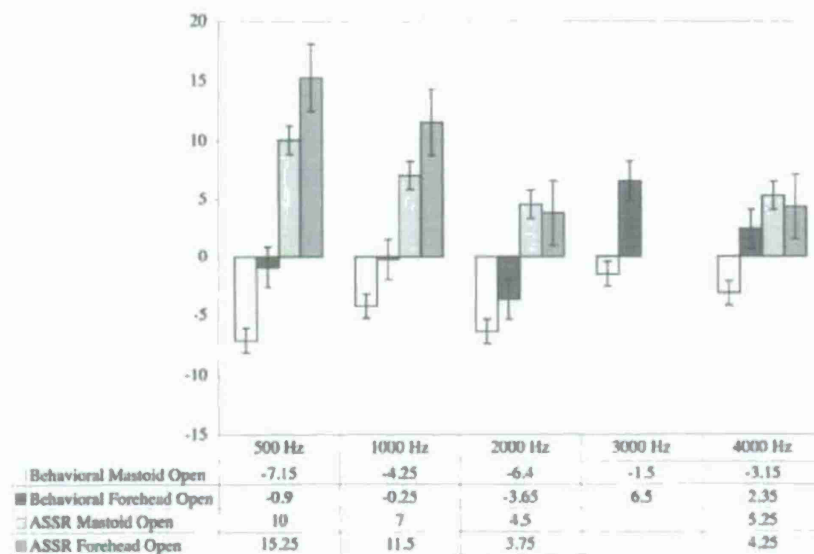|	500 Hz	1000 Hz	2000 Hz	3000 Hz	4000 Hz
Behavioral Mastoid Open	-7.15	-4.25	-6.4	-1.5	-3.15
Behavioral Forehead Open	-0.9	-0.25	-3.65	6.5	2.35
ASSR Mastoid Open	10	7	4.5		5.25
ASSR Forehead Open	15.25	11.5	3.75		4.25

Figure 25. Intensity (dB HL) for ear canals open: Intensity dB HL. Note: Poorer thresholds, positive values, correspond to ASSR (a supra threshold measure).

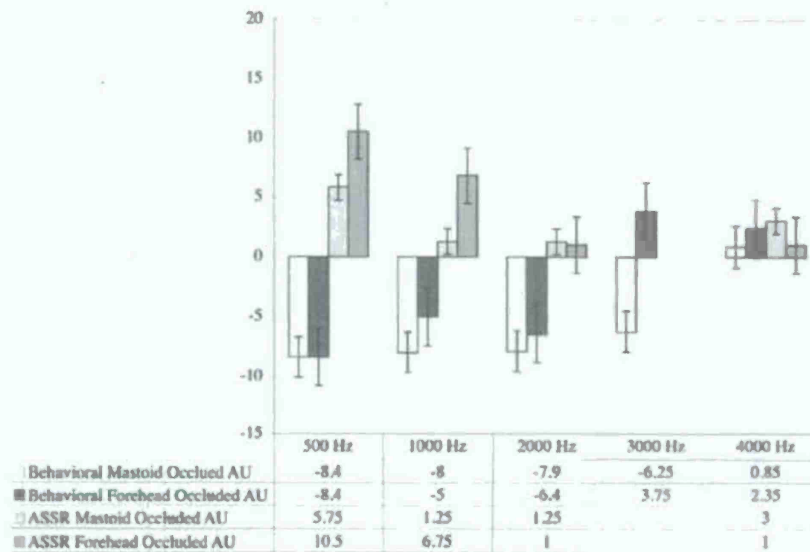|	500 Hz	1000 Hz	2000 Hz	3000 Hz	4000 Hz
Behavioral Mastoid Occlued AU	-8.4	-8	-7.9	-6.25	0.85
Behavioral Forehead Occluded AU	-8.4	-5	-6.4	3.75	2.35
ASSR Mastoid Occluded AU	5.75	1.25	1.25		3
ASSR Forehead Occluded AU	10.5	6.75	1		1

Figure 26. Intensity (dB HL) for ear canals closed: Intensity dB HL Note: Poorer thresholds, positive values, correspond to ASSR (a supra threshold measure). AU denotes both ears were occluded

Conclusions: The data from all three measures are consistent with the occlusion effect, that is, occluding the ear canals modifies bone conduction propagation. Simulations and functional models of bone conduction propagation must account for the occlusion phenomenon. The results obtained from this portion of the project provide representative values that could be used for further development and verification (Brault et al., 2007; Wismer et al., 2008).

6.2. Behavioral bone conduction thresholds as a function of static force, oscillator placement location, and head size

Purpose: The purpose of the study was to determine whether bone conduction hearing thresholds differ for oscillator placement location if static contact force is held constant. Thresholds for bone conduction hearing are determined with a bone oscillator using a standard headband designed to apply 5.4N of static force to the oscillator (ANSI S3.6-1996 R2004) in clinical settings. In actual practice, however, the static contact force varies over a range of several Newtons, as the headband is stretched to accommodate head size and oscillator placement location (e.g., mastoid or forehead) or if the headband is modified for use with young children or for comfort. Typically, thresholds of bone conduction at the forehead are less sensitive than those at the mastoid, however the contact force to couple the oscillator to the head at these placement locations differs. Therefore the relation, if any, between placement location, contact force and hearing threshold sensitivity is not clear.

Procedure: A total of 24 normal hearing participants (12 male, 12 female) took part in the experiment. Participants were separated into two groups (small and large) based upon head size. There were 12 participants in the small head group and 12 participants in the large head group. Head size measures were made from nasion to inion using calipers and tape measure. Head circumference measures were made using the CDC guidelines and the International 10-20 system. Behavioral bone conduction thresholds were obtained in 1-dB steps from 250 Hz to 8000 Hz in 1/6 octave bands at three placement locations: right mastoid, left mastoid and forehead. Three static force levels were evaluated; 2N, 5N, and variable. The variable force levels were produced by the Standard clinical bone-conduction headband (ANSI S3.6-1996 R2004). For each participant, the static force levels applied by the standard headband were measured. The 2N and 5N force levels were produced by customized headbands which had been fabricated and calibrated (See Section 7) to provide a known static force applied to the oscillator when coupled to the head.

Results Summary: Data from the small head group showed the mean threshold for variable force was 1.48 dB HL, for 2N was 3.14 dB HL, for 5N was 3.72 dB HL. Mean thresholds by placement were 5.87 dB HL at forehead, 1.51 dB HL at left mastoid, and 0.96 dB HL at right mastoid. Mean thresholds by frequency showed that 2000 Hz (8.81 dB HL) was significantly higher than other frequencies. There was no effect of gender and no interaction.

Data from the large head group showed the mean threshold for variable force was 0.51 dB HL, for 2N was -0.45 dB HL, for 5N was 6.72 dB HL. Mean thresholds by placement were 3.28 dB HL at right mastoid, 2.69 dB HL at forehead, and 0.81 dB HL at left mastoid. Mean thresholds by frequency showed that 2000 Hz (6.50 dB HL) was significantly higher than other frequencies. There was no effect of gender; however there was an interaction between force by head size and an interaction between placements by head size.

The group of graphs, Figure 27, display the interaction between force by head size and placement by head size. A significant interaction was found for the large head group, but not for the small head group.

The second group of graphs, Figure 28, displays bone conduction behavioral threshold as a function of force for the small and large head listeners. (Please note: About 3% of all thresholds collected were at the limits of the audiometer (-10 dB HL) and thus were replaced with median values for the group.) The static force levels were greater for the large head group than the small head group. Forehead placement yielded greater force than mastoid placement for both groups.

Interaction of Force by Headsize Group

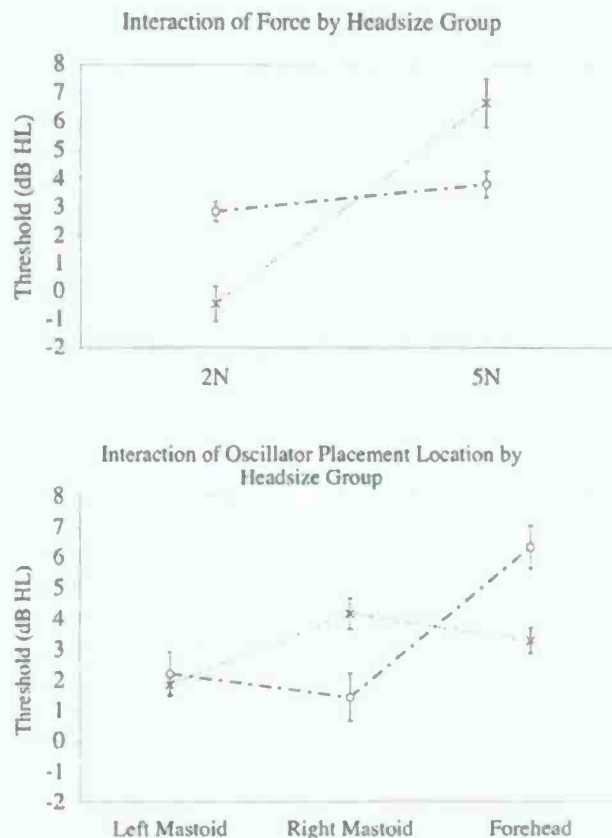Interaction of Oscillator Placement Location by Headsize Group

Figure 27. Large and small head group data for differences in two static force levels and three oscillator locations. Group Two Graphs Key: Small head = circle; Large head = X
SEM= I

Conclusions: Mean behavioral bone conduction thresholds obtained with the standard headband, that produced variable static force levels, were not related to the static force level in the small or large head size group. Forehead oscillator placement yielded thresholds that were less sensitive than mastoid placement. This is in agreement with previous research (Dirks and Malmquist, 1969). For the calibrated force levels of 2N and 5N the small head group did not show a significant difference between mean thresholds obtained and again forehead placement yielded the least sensitive thresholds.
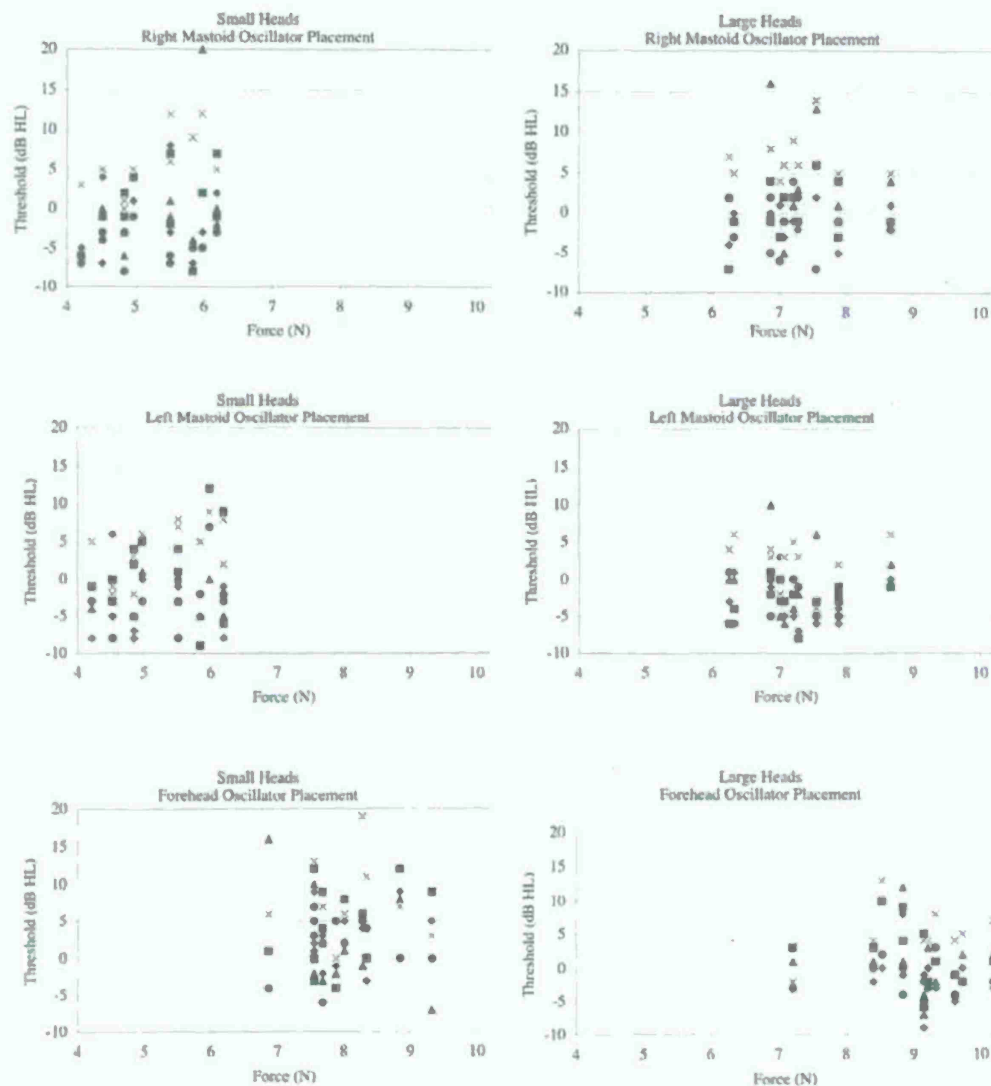
Figure 28. Behavioral thresholds by static force across four frequencies as a function of oscillator placement with the standard headband in groups of adults with small vs. large head size. Group One Graph Symbol Key: 1 kHz = diamond 1.5 kHz = triangle 2 kHz = X 3 kHz = circle 4 kHz = square

These results indicated that the standard clinical headband used for bone conduction testing is capable of producing a range of static force levels that is dependent on oscillator placement location and the listener's head size. For the small head group, oscillator placement location seems to have an affect on bone conduction behavioral thresholds, although static force does not.

- 34 -

The large head group showed a different pattern of results for the calibrated force levels. Mean behavioral thresholds at 5N were less sensitive than those obtained at 2N. Right mastoid thresholds were less sensitive than forehead thresholds. In order to further investigate the different pattern of results obtained for the large head group, a subset of large headed listeners were re-tested in a follow-up pilot experiment (See Section 6.3).

6.3. Behavioral bone conduction thresholds as a function of static force and oscillator placement location for large heads (Pilot study)

Purpose: A subset of 5 large headed listeners were re-tested and the repeatability of the results obtained in the initial experiment (See Section 6.2) were thus documented. In addition to the 2N and 5N levels of static force, three additional calibrated force levels (3.5N, 6N and 8N) were also tested. This was done in order to examine the pattern (i.e. linear, curvilinear, etc.), if any, between force and threshold in large headed listeners.

Procedure: Five listeners (1 female, 4 male) from the large head group who had participated in the initial experiment (See Section 6.2) were tested. Behavioral bone conduction thresholds were obtained in 1 dB steps from 250 Hz to 8000 Hz in 1/6 octave bands at three placement locations: right mastoid, left mastoid and forehead. Five static force levels were evaluated; 2N, 3.5N 5N, 6.5N and 8N.

Results Summary: Data from the re-test of 5 large headed listeners showed mean thresholds of 1.01 dB HL for 2N; -0.12 dB HL for 3.5 N; 0.84 dB HL for 5 N; -0.20 dB HL for 6.5 N; and -0.28 dB HL for 8N. Mean thresholds for each placement were 4.40 dB HL at the forehead, -2.18 dB HL at the left mastoid, and -2.47 dB HL at the right mastoid. Mean threshold for frequency showed that 4000 Hz (-4.01 dB HL) was significantly lower than other frequencies.

Conclusions: The data obtained from the re-test of 5 large headed listeners showed no significant difference between the mean behavioral thresholds obtained with the 5 calibrated static force levels. Forehead placement yielded the least sensitive thresholds. These results are not in agreement with those obtained in the initial experiment (See Section 6.2), however fewer participants were tested. Additional re-testing of large headed listeners is warranted in order to more fully determine if static force and head size are related in listeners with large heads (Brault et al., 2008).

6.4. Summary of human subject testing

Experimental evidence from behavioral tests of hearing sensitivity (threshold measures) and physiologic responses (supra-threshold Auditory Steady-State Response, ASSR) were evaluated with the ears open and closed (occluded). The ASSR was chosen instead of the ABR because the spectra of these stimuli used to obtain the ASSR are more frequency specific than those used to obtain auditory brain stem response (ABR) measures. Further, in general the results from ASSR are in excellent agreement with behavior thresholds for both high and low frequencies. In addition, its acquisition time is considerably shorter than ABR, further enhancing its accuracy. In addition, the RMS

sound pressure levels measured in the ear canals (Real Ear Measures) were evaluated with ear canals open and closed. It was not necessary to purchase a new Real Ear Probe-Tube system for this project, because a system currently used in the clinic became available. Measurement setting and protocols were modified, in consultation with the manufacture's research and development team, to use bone-conducted stimuli. The comprehensive data were used to validate the computational model of bone conduction propagation in the skull. Numerical and experimental results showed that the occlusion effect is more prevalent at low frequencies and decreases as frequency increases. The results indicated that the occlusion effect is nearly absent at 2 kHz and at higher frequencies.

Bone conduction hearing sensitivity is greater for oscillator placement at the mastoid region compared to the forehead, consistent with previous research (Dirks and Malmquist, 1969). On average, for groups of individuals with small head size, bone-conduction hearing sensitivity was independent of the static force applied to the oscillator. Results for groups of individuals with large head size were more variable with greater individual differences and in test-retest reliability. Pilot results for a small number of large headed adults were inconsistent upon retest and should be investigated in future work.

7. HEAD BAND FORCE CALIBRATION FOR BONE CONDUCTION STUDIES

A set of headbands were fabricated and calibrated for bone conduction experiments. For these experiments, it was necessary to maintain a known bone conductor contact force across subjects, and different measuring points. The headbands were made to produce known forces for varying stretch distances d (Figure 29). A system of calipers was devised to quickly obtain the distance d from a subject, and match it with the headband that would most closely provide the desired force.
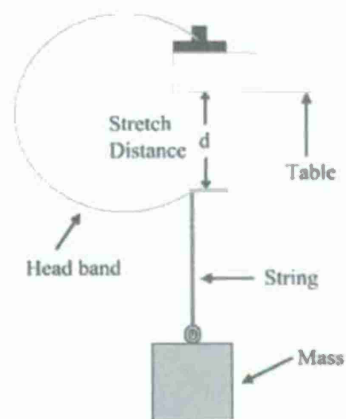

Figure 29. Headband calibration setup.

For each headband, a force versus distance relationship was obtained. The headband was positioned on the border of a table with one end attached to a variable weight. The force was obtained using Newton's second law $F = mg$ where g is the acceleration due to gravity (9.81 m/s^2). A weight of 204 g is therefore equivalent to 2N of force. The stretch distance d as measured and recorded.

A total of five headbands were calibrated: four custom, and one standard (used in Section 6 studies). Force measurements between 2N and 5N were obtained for each custom headband, and between 2N and 10N for the standard headband (Figure 30).

The results show that with the custom headbands, forces between 2N and 5N can be easily achieved at a generous range of distances. The standard headband force to distance relation shows that it always exerts more force than the custom head bands for a given distance.
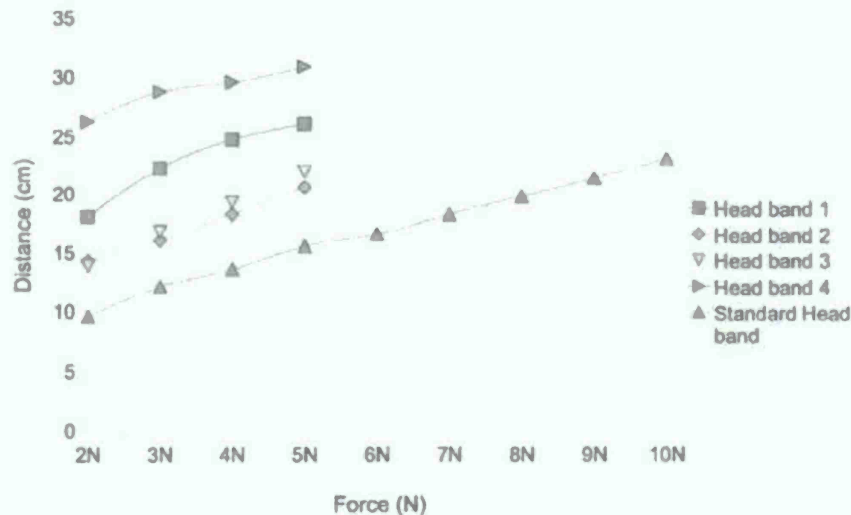

Figure 30. Force vs. distance plots for four custom head bands and the standard head band.

8. OVERALL CONCLUSIONS

The highly interdisciplinary program has addressed successfully the challenging technical goal set forth to develop and validate an acoustic wave propagation model using well understood and documented computational techniques that track an air-borne incident acoustic wave propagated around, into and in the human head.

A finite element model was formulated for simulating the acoustic wave propagation into concentric spheres. This model was verified against the closed form

solution of the plane wave propagation into concentric fluid spheres.

A ray tracing method was developed and verified to visualize the acoustic wave propagation pathways from a scalar pressure field.

Finally, the occlusion effect provides a relatively robust phenomenon to compare the computational findings (Table 3) with the behavioral and functional findings (Figures 22 and 23). The contour (or difference score) between the open and occluded ear is shown in Figure 31 and shows a similar trend between the computational findings and the behavioral and functional findings. The similarity is more clearly shown with the normalized (at 1 kHz) difference score (Figure 32).

In conclusion, the computational approach, utilizing fluid elements, provides very good agreement with human subject findings.
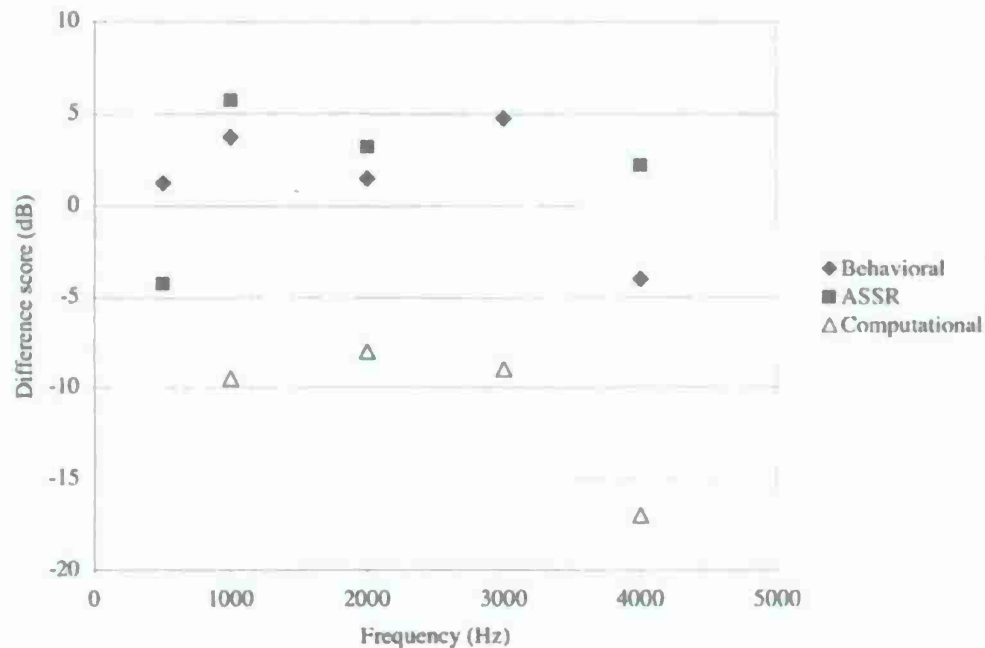

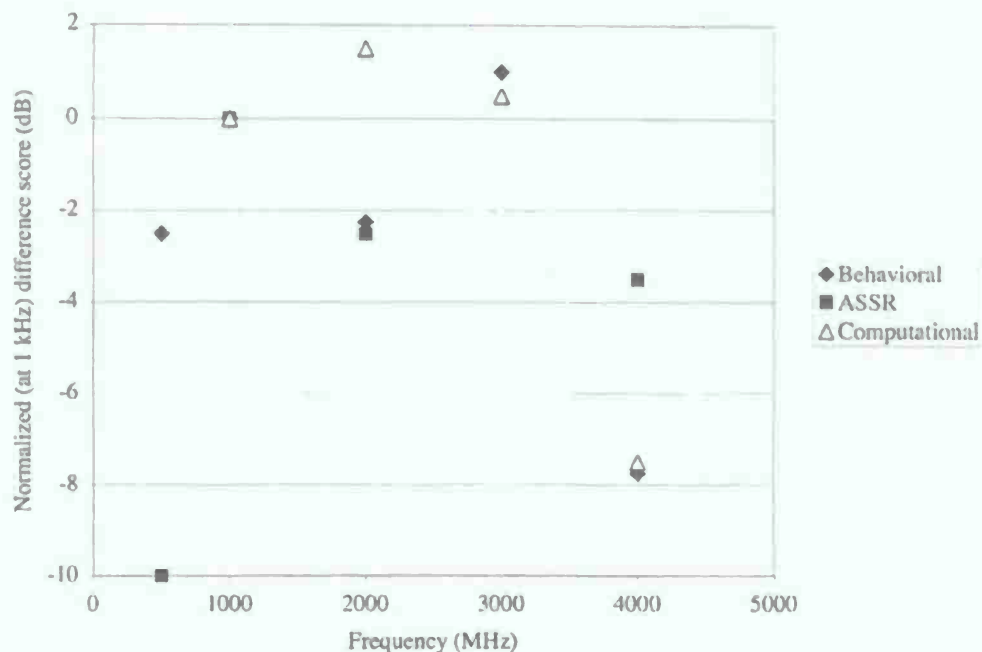Figure 31. Contour (or difference score) as a function of frequency.

Figure 32. Normalized contour (or normalized difference score) as a function of frequency.

9. LIST OF PUBLICATIONS

B. A. Auld (1990). Acoustic Fields and Waves in Solids, Volumes I and II, Second Edition, Krieger Publishing Company, Marabar, FL

A. A. Bellina (2009). Applying Computational Techniques to Obtain the Acoustic Pathways into the Human Head: MS Thesis, Department of Electrical and Computer Engineering, University of Illinois, Urbana, IL.

L. M. Brault, W. Han, C. Lansing, R. C. Chambers, J. McNew, A. Bellina and W. D. O'Brien, Jr. (2008). Influence of static force on bone conduction threshold measurement [Abstract-1pPP15], *Journal of the Acoustical Society of America*, 124, 2456.

L. M. Brault, C. Lansing, R. C. Chambers and W. D. O'Brien, Jr. (2007) Examination of bone conducted sound pathways [Abstract- 4aPP12], *Journal of the Acoustical Society of America*, 122, 3063.

D. Dirks and C. Malmquist (1969). Comparison of frontal and mastoid bone-conduction thresholds in various conduction lesions. *Journal of Speech and Hearing Research*, 12, 725-746.

J. A. McNew (2008). Application of Acoustic Ray Tracing to Determine Sound Pathways into the Human Head. MS Thesis, Department of Electrical and Computer Engineering, University of Illinois, Urbana, IL.

J. McNew, A. Bellina and W. D. O'Brien, Jr. (2008). Applying acoustic ray tracing from the full wave equation solution to determine the nonair conduction pathways into the human head [Abstract-1pPP12], *Journal of the Acoustical Society of America*, 124, 2456.

J. A. McNew, R. Lavarello and W. D. O'Brien, Jr. Sound Scattering from Two Concentric Fluid Spheres. *Journal of the Acoustical Society of America*, in press

J. McNew and W. D. O'Brien, Jr. (2008). Sound scattering from two concentric fluid spheres [Abstract-2aPP9], *Journal of the Acoustical Society of America*, 122, 2968.

A. D. Pierce (1989). Acoustics: An Introduction to its Physical Principles and Applications. McGraw Hill, New York, NY.

M. Wismer, L. M. Brault, S. Melamed, C. Lansing, R. C. Chambers and W. D. O'Brien, Jr. (2007) Numerical and experimental study of bone conducted sound and the occlusion effect [Abstract- 5aPP15], *Journal of the Acoustical Society of America*, 121, 3198.

M. Wismer and W. D. O'Brien, Jr. (2008). Simulation of bone-conducted sound pathways to the inner ear [Abstract-1pPP13], *Journal of the Acoustical Society of America*, 124, 2456.